Mon. Not. R. Astron. Soc. **000**, 1–23 (2009) Printed 3 February 2009 (MN LATEX style file v2.2)

A new search for distant radio galaxies in the Southern hemisphere – II. 2.2μm imaging

J. J. Bryant[1⋆], J. W. Broderick[1], H. M. Johnston[1], R. W. Hunstead[1], B. M. Gaensler[1,2], and C. De Breuck[3]
[1] *Institute of Astronomy, School of Physics A29, The University of Sydney, NSW 2006, Australia*
[2] *Harvard-Smithsonian Center for Astrophysics, 60 Garden Street, Cambridge MA 02138, USA*
[3] *European Southern Observatory, Karl Schwarzschild Straße 2, D-85748 Garching, Germany*

arXiv:0902.0643v1 [astro-ph.CO] 3 Feb 2009

ABSTRACT

We have compiled a sample of 234 ultra-steep-spectrum (USS) selected radio sources in order to find high-redshift radio galaxies. The sample covers the declination range $-40^\circ < \delta < -30^\circ$ in the overlap region between the 1400-MHz NRAO VLA Sky Survey, 408-MHz Revised Molonglo Reference Catalogue and the 843-MHz Sydney University Molonglo Sky Survey (the MRCR–SUMSS sample). This is the second in a series of papers on the MRCR–SUMSS sample, and here we present the K-band (2.2μm) imaging of 173 of the sources primarily from the Magellan and the Anglo-Australian Telescopes. We detect a counterpart to the radio source in 93 per cent of the new K-band images which, along with previously published data, makes this the largest published sample of K-band counterparts to USS-selected radio galaxies. The location of the K-band identification has been compared to the features of the radio emission for the double sources. We find that the identification is most likely to lie near the midpoint of the radio lobes rather than closer to the brighter lobe, making the centroid a less likely place to find the optical counterpart. 79 per cent of the identifications are less than 1 arcsec from the radio lobe axis. These results differ from studies of low-redshift radio samples where the environments are typically not nearly so dense and disturbed as those at high redshift. In contrast to some literature samples, we find that the majority of our sample shows no alignment between the near-infrared and radio axes. Several different morphologies of aligned structures are found and those that are aligned within 10 degrees are consistent with jet-induced star formation. The distribution and median value of the K-band magnitudes for the MRCR–SUMSS sample are found to be similar to several other USS-selected samples even though each sample has a very different median 1400 MHz flux density. USS-selection from a lower-radio-frequency sample has not netted fainter K-band magnitudes, which may imply that the k-correction is not responsible for the effectiveness of USS-selection. Due to space constraints, lower resolution figures are shown here, and the full resolution is available in the MNRAS published paper.

Key words: galaxies: active – surveys – galaxies: high-redshift – infrared: galaxies – radio continuum: galaxies.

1 INTRODUCTION

At low-redshift, powerful radio galaxies are hosted by giant ellipticals (Matthews, Morgan & Schmidt 1964). The inference that high-redshift radio galaxies (HzRGs; $z > 2$) host a supermassive ($> 10^9$ M$_\odot$) black hole (Blandford & Payne 1982), and the close connection between the mass of the black hole and that of the galaxy (e.g. Gebhardt et al. 2003), provides an evolutionary path to the present-day giant ellipticals. HzRGs are therefore excellent laboratories for studying the evolution of massive galaxies.

Most HzRGs found to date have been selected on the basis of their steep radio spectral index α (where $S_\nu \propto \nu^\alpha$ for flux density S at frequency ν), since ultra-steep-spectrum (USS; $\alpha < -1.0$) radio galaxies are more likely to be found at $z > 2$ (Blumenthal & Miley 1979; Tielens, Miley & Willis

⋆ E-mail: jbryant@physics.usyd.edu.au

1979; De Breuck et al. 2000, 2006). The physical basis for this so-called $z-\alpha$ correlation was previously thought to be due to a concave radio galaxy spectrum that was assumed to steepen to higher frequencies. The steeper part of the spectrum would be redshifted, giving a steeper spectral index at a given observed frequency for a high-redshift source than a low-redshift one. However, this interpretation has recently been challenged by Klamer et al. (2006) who introduced a new paradigm for interpreting the radio spectra of high-redshift massive galaxies, in which USS massive galaxies are located in extremely dense environments, comparable to rich clusters of galaxies in the local Universe. The high ambient gas density in this environment means that the radio lobes are pressure-confined and lose their energy slowly by synchrotron and inverse Compton losses (rather than rapidly by adiabatic expansion as occurs in more rarefied environments at low redshift). If this interpretation is correct, then not only do radio galaxies represent the extreme limit of the galaxy mass function at early times, they may also locate the most extreme overdensities of matter in the early Universe.

The number density of HzRGs is low, only a few times $10^{-8}\,\mathrm{Mpc}^{-3}$ (Venemans et al. 2007). Of these, 96 per cent are detected to $K = 22$ (Miley & De Breuck 2008) and hence a K-band survey is an efficient method of identifying the hosts of USS radio-selected galaxies. The spectral energy distribution of old ($> 1\,\mathrm{Gyr}$) stars peaks in the near-infrared at low redshift, while that of young blue stars dominates the K-band at high redshift, and therefore it has been argued that the K-band emission can be assumed to trace the stellar mass. HzRGs have the highest K-band luminosities in the early Universe, and are brighter than optically-selected galaxies at all redshifts, which demonstrates that radio galaxies are among the most massive galaxies at all epochs (Rocca-Volmerange et al. 2004; Seymour et al. 2007). Furthermore, they follow a well-known linear[1] correlation between redshift and K magnitude, the K–z relation (Lilly & Longair 1984), which is an efficient tool for filtering out the low-redshift galaxies, leaving a smaller sample of potential high-redshift objects for follow-up spectroscopy.

We have carried out a search in the Southern Hemisphere designed to find high-redshift ($z > 2$) radio galaxies, to study their evolution, and to form a significant sample of those at $2 < z < 3.5$ for a detailed quantitative study of their environments. This is the first survey in the South to use sensitive low-frequency catalogues to data mine a large area of sky, and it became possible with the completion of the 843-MHz Sydney University Molonglo Sky Survey (SUMSS; Bock et al. 1999; Mauch et al. 2003) and the reanalysis of the 408-MHz Molonglo cross data (Large et al. 1981) to give the Revised Molonglo Reference Catalogue (MRCR; Crawford, private communication).

The details of the sample selection and the radio imaging results were given in Broderick et al. (2007, hereafter Paper I). The present paper discusses the K-band identifications and magnitudes for 173 of the radio sources in Paper I, along with new higher-resolution radio images. The optical spectra for sources from the MRCR–SUMSS sample are introduced in Bryant et al. (2008, hereafter Paper III) which presents a detailed analysis of the radio, K-band and redshift information for the sample. We have adopted a flat, Λ cold dark matter cosmology with $H_0 = 71$ km s^{-1} Mpc^{-1}, $\Omega_\mathrm{M} = 0.27$ and $\Omega_\Lambda = 0.73$.

[1] Linear fit between $\log(z)$ and K magnitude corresponds to a power-law relation between z and 2.2μm flux.

2 OBSERVATIONS AND DATA REDUCTION

2.1 Target selection

The sources for our survey were selected by cross-matching
(i) the 843-MHz SUMSS catalogue,
(ii) the 408 MHz MRCR, which lowered the earlier MRC flux density limit of 0.95 Jy to ∼200 mJy (5σ), and
(iii) the 1400-MHz NVSS (Condon et al. 1998) in the overlap region with SUMSS (declination $-30°$ to $-40°$).

We then selected sources with a spectral index between 408 to 843 MHz, $\alpha_{408}^{843} < -1.0$ and $|b| > 10°$ (to avoid confusion from the Galactic plane). Double lobed sources were inspected by eye to ensure that both components were included in the flux density measure. Minimum flux density cut-offs of 200mJy and 15mJy were applied to the MRCR and NVSS catalogues respectively to improve the accuracy of the spectral indices.

The target selection is discussed in detail in Paper I.

2.2 Radio observations - ATCA

2.2.1 1384- and 2368-MHz imaging

Radio images were obtained with the Australia Telescope Compact Array (ATCA) in several runs in 2003–2006. Both 1384- and 2368-MHz images were needed to pinpoint the K-band identification. The full details of the radio observations and reduction are given in Paper I where the analysis was done with natural-weighted images. However, in this paper, in cases where the K-band counterpart was not clear, we used uniform-weighted images as they have better resolution of $\sim 6.1 \times 3.5\,\mathrm{arcsec}^2$ at 2368 MHz.

2.2.2 4800- and 8640-MHz imaging

Higher-resolution observations were obtained for 29 sources on UT 2008 January 16 – 20. Dual-frequency observations at 4800 and 8640 MHz were carried out with a 2×128 MHz bandwidth correlator configuration. The 6A array configuration was used, spanning baselines from 337 to 5939 m. The median integration time per source was ∼70 min, consisting of well-spaced cuts of 3–4 min in duration. PKS B1934−638 was used as the primary calibrator, while phase calibrators were observed every 20 min. A log of observations for the 4800- and 8640-MHz data is given in Table 1.

The data were reduced with MIRIAD (Sault, Teuben & Wright 1995), following a procedure similar to that described in Paper I. We used natural weighting to optimise the sensitivity; the median angular resolution is 4.2×2.9 arcsec^2 at 4800 MHz and 2.3×1.6 arcsec^2 at 8640 MHz. CLEAN boxes were defined using both the automatically constrained CLEAN technique described in Paper I, and manual selection where necessary. After the CLEAN regions had been defined, each dirty image was CLEANed to 2–3 times the theoretical rms noise level; typically only ∼100 iterations were necessary. Phase-only

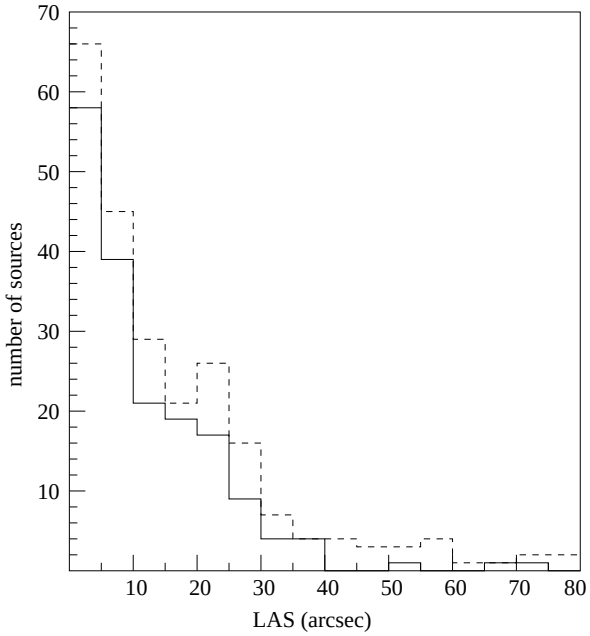

Figure 1. Distribution of the largest angular size from the 2368-MHz images (or 4800- or 8640-MHz images where available) for all of the MRCR–SUMSS sources from Paper I (dashed line) and from Table 2 for the objects that were imaged in K-band (solid line).

self-calibration was then used to improve the dynamic range. The median rms noise levels are 0.14 mJy beam^{-1} at 4800 MHz and 0.20 mJy beam^{-1} at 8640 MHz; the measured rms noise level is in close agreement with the theoretical value in all but a handful of the CLEAN images. We estimate that the typical positional uncertainty is < 0.5 arcsec at both 4800 and 8640 MHz. However, in a handful of cases, the positional uncertainty may be up to $\sim$0.5 arcsec at 8640 MHz because of poor phase stability.

2.3 K-band (2.2μm) observations

The K-band observations are listed in the log of observations in Table 1. A Ks filter was used for the K-band imaging.

Of the 234 sources with radio imaging, two already have 2MASS magnitudes and we have selected a further 163 sources for K-band imaging. In addition, there are eight targets in our sample that have previously been observed by De Breuck et al. (2004). The selection of sources for K-band followup was primarily based on the Right Ascensions accessible during the observing sessions, and hence there is no bias in the K-band sample compared to the radio sample. There was no selection made on the basis of flux density or radio morphology. Fig. 1 shows that the sources chosen for K-band imaging are representative of the largest angular size (LAS) distribution of the whole radio sample.

2.3.1 IRIS2

Our initial Ks-band imaging was begun on the 3.9-m Anglo-Australian Telescope's (AAT) IRIS2 detector (Gillingham & Jones 2000). With a scale of 0.446 arcsec pixel^{-1}, the 1024×1024 pixel HAWAII HgCdTe array imaged a sky area of 8×8 arcmin^2. Two observing runs on 2004 August 3–5 and 2005 June 21–24 were mostly clouded out. We did, however, obtain Ks-band images of 42 sources in seeing of 0.9–1.9 arcsec. Integration times were 15 mins, made up of 8 cycles of 8 s exposures in a 14-point random jitter pattern. There were seven non-detections, of which five were reobserved on the larger Magellan telescope, as discussed in Section 2.3.2.

The data were reduced with the pipeline data reduction package, ORACDR, which sky-subtracted, flat-fielded, shifted and combined the individual dithered images. The faintest objects measured had $Ks = 19.6$.

2.3.2 PANIC

We observed 126 targets in Ks-band with Persson's Auxiliary Nasmyth Infrared Camera (PANIC; Martini et al. 2004) on the 6.5-m Magellan Baade telescope at Las Campanas Observatory on 2006 June 11–13, 2006 November 8–10 and 2007 April 2–4. These included five objects that remained undetected in IRIS2 images and two targets which were undetected in previous NTT observations (see De Breuck et al. 2004). The field of view is 2×2 arcmin^2 from the 1024×1024 pixel HgCdTe Hawaii detector with 0.125 arcsec pixel^{-1}. Seeing in the optical ranged from 0.6–0.8 arcsec for most of the three observing runs, only briefly exceeding 1.0 arcsec, and at best reaching just under 0.5 arcsec. The conditions were photometric apart from two hours of thin cirrus in the 2006 June run. We used a 9-point dither pattern of 20-s exposures and repeated this pattern with three loops giving an exposure time of 9 mins. Reduction was done in real time and if the object was not detected in 9 mins, the integration was repeated.

We had intermittent problems with moon glow causing slight to very strong stripes across the image. This was mostly due to reflection of the moon off the telescope baffles. In the 2006 November run we had brief periods of interference in the images due to an electronics problem. Both of these issues were short lived and when they occurred they affected only some of the nine dithered images. In those cases, the nine images were carefully inspected, and only the clean dithers were combined. Hence, some of the integration times for PANIC images are not multiples of 9 mins (see Table 2).

Reduction was done using the GOPANIC reduction pipeline routine, which is part of the PANIC package in IRAF by P. Martini. The pipeline summed the individual exposures, applied a linearity correction, flat fielded and sky subtracted the images, did a distortion correction then shifted and added the individual dithered images into a final frame. When multiple dither sequences were done, the shifts measured in IRAF CENTERS were used in IRAF IMCOMBINE to make the final image. The deepest images reached $Ks = 21.5$ (in just under 1 hr integration). Counterparts for nine sources were not detected.

2.3.3 Astrometry

Accurate coordinates were applied to the final IRIS2 and PANIC images by comparison with the SuperCOSMOS Sky

Table 1. Log of observations.

Date	Telescope	Instrument	Optical seeing (arcsec)
***K*-band imaging:**			
2004 August 3–5	AAT	IRIS2	0.9–1.9
2005 June 21–24	AAT	IRIS2	0.9–1.9
2006 June 11–13	Magellan	PANIC	0.5–1.5
2006 November 8–10	Magellan	PANIC	0.5–1.3
2007 April 2–4	Magellan	PANIC	0.5–1.0
4800- & 8640-MHz imaging:			
2008 January 16–20	ATCA		

Survey (Hambly et al. 2001) images using the KARMA[2] astrometry package (Gooch 1996) KOORDS. The SuperCOSMOS astrometry is accurate to $\leqslant$ 0.2-arcsec rms. There are several fields at high Galactic latitude with larger astrometric uncertainties; these fields have as few as three stars in the PANIC field of view. The majority of fields had more than seven stars suitable for astrometry.

The astrometric accuracy on the Ks-band images was sufficient in most cases to identify the counterpart to each radio source. Of the 11 sources (9 from PANIC and 2 from IRIS2) without a K-band identification, it is most likely that the identifications are simply fainter than the image limit or the radio structures are extended with ambiguous identifications. The non-detections are discussed further in Section 3.2. We are confident that the non-detections are not due to astrometric misalignment.

2.3.4 K-band photometry

Two of the objects already had K-band magnitudes listed in the Two Micron All Sky Survey (2MASS; Skrutskie et al. 2006) and therefore did not need to be reobserved. Both the PANIC and IRIS2 imaging was done through a Ks-band filter as were the 2MASS images. The differences among Ks filters are much smaller than the magnitude errors and have therefore been ignored. As we do not have any colour information and the effect is very small, we have not converted Ks-band magnitudes to K-band. For simplicity, we refer hereafter to the magnitudes as K rather than Ks.

Photometry was done in IRAF RADPROF using stars from the 2MASS point source catalogue. In most fields there were at least four 2MASS stars which were used for calibrating our photometry. Because of their smaller fields of view, there were six PANIC fields which had only two suitable 2MASS stars, two fields had one and one field had no suitable 2MASS stars. Therefore, all of the 2MASS stars measured in the images were plotted against the PANIC measured magnitudes, and a best fit line was used to calibrate the frames that had fewer than four 2MASS stars. Even in the cases where there were four 2MASS stars to calibrate an individual field, the photometry agreed, within errors, with the best fit line for all stars across all fields. In each case, the resultant errors were carefully assessed based on the photometry fitting errors and the offset errors from fitting 2MASS stars.

Several of the PANIC fields were affected either by some cloud, or by reflections of moonlight onto the detector leading to uneven backgrounds. Stray light on one quadrant of the IRIS2 chip gave background variations in some IRIS2 frames. In these cases the photometric errors are substantially higher.

An airmass correction was not applied as all images had an airmass < 2 and the correction was small compared to the errors. No Galactic extinction correction was applied as fewer than 30 of our sources have $|b| < 20^{\circ}$.

All of the identifications were compact at K-band, such that a 4-arcsec-diameter aperture was sufficient to contain each source without contamination from nearby objects.

3 RESULTS

Fig. 2 shows the ATCA 2368-MHz contours from Paper I, overlaid on the K-band images, for a selection of our sources, including those discussed individually in Section 3.2 and in Paper III. Overlay plots for the remainder of our sources can be found in the Appendix.

Table 2 lists the data for the objects we observed in K-band, or for which we have an identification which has been followed up with spectroscopy (presented in Paper III). Some sources not only met our selection criteria, but were also part of the SUMSS–NVSS sample (De Breuck et al. 2004; Paper I) and were therefore not reobserved. For those sources, the K-band magnitudes and positions given are from De Breuck et al. (2004).

The columns in Table 2 are as follows:
(1) NVSS source name.
(2) and (3) K-band magnitude in 4-arcsec- and 8-arcsec-diameter apertures respectively. For sources marked SC, no K-band image was obtained as a faint SuperCOSMOS identification was found in our overlay plots following the ATCA imaging. "—" means that a K magnitude could not be measured in an 8-arcsec aperture because of a nearby source or because of the sky brightness surrounding very faint sources.
(4) and (5) RA and DEC (J2000) of the K-band identification. Sources that had no K-band or SuperCOSMOS identification are marked "—".
(6) K-band image exposure time in minutes.
(7) The origin of the K-band image. PANIC is on the Magellan Baade Telescope, and IRIS2 is on the AAT. 'DB' refers

[2] http://www.atnf.csiro.au/computing/software/karma/

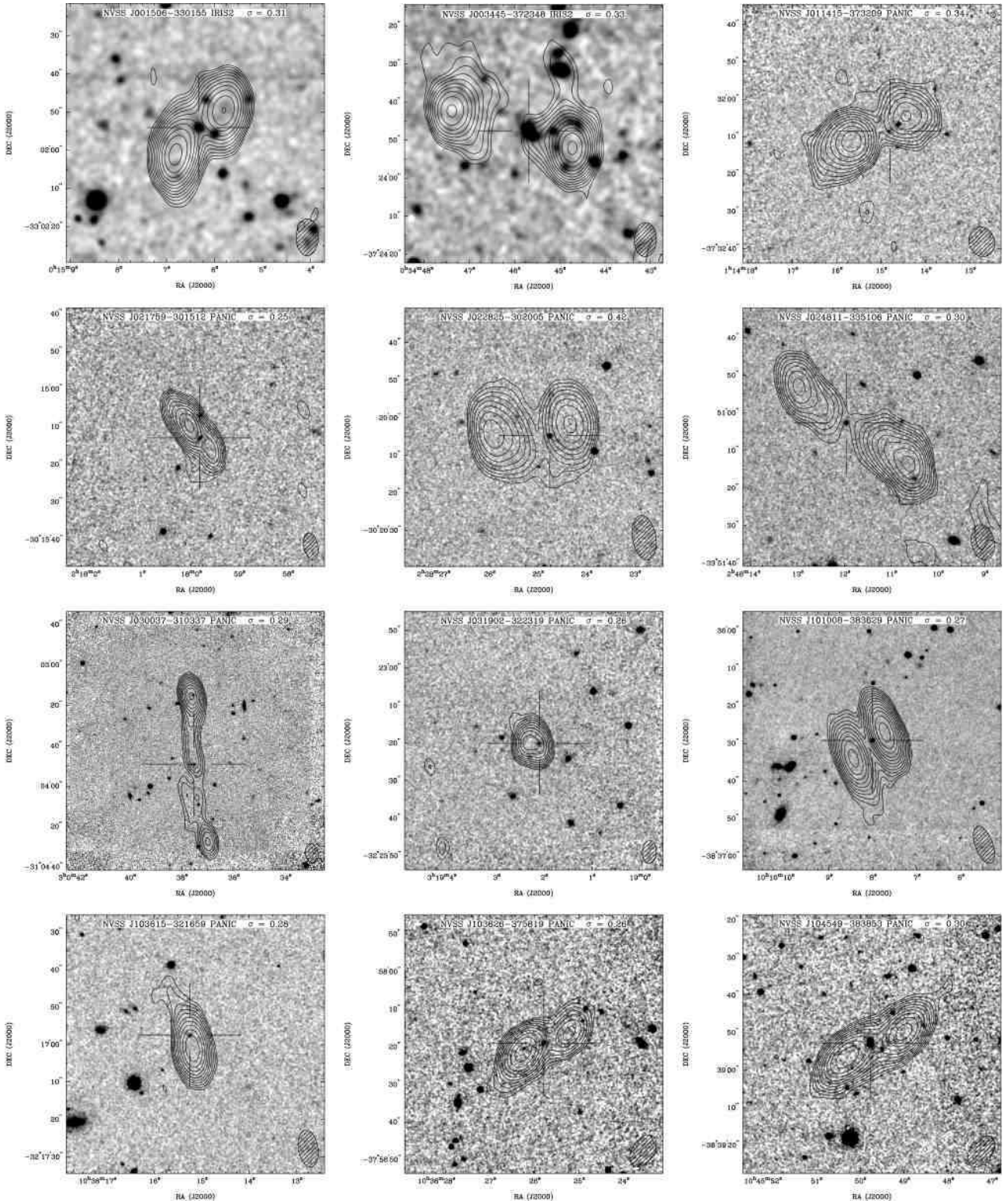

Figure 2. 2368-MHz ATCA contours overlaid on the K-band images for a selection of our sample, including the sources discussed in Section 3.2 and those with both PANIC or IRIS2 images and spectra which will be discussed further in Paper III. Overlay plots for the remainder of the K-band sample can be found in the Appendix. The K-band images show in the header which instrument they are from. They have been smoothed using a gaussian kernel of 3 pixels FWHM for the PANIC and IRIS2 images, and 2 pixels FWHM for the 2MASS images. All the radio contours are from natural-weighted images except NVSS J021759−301512, NVSS J031902−322319 and NVSS J142320−365027 which have uniform weighting and slightly higher resolution. The lowest contour is 3 sigma, and the contours are a geometric progression in $\sqrt{2}$. The rms noise (σ) is shown in the header of each image in mJy beam^{-1}. Crosshairs mark the K-band counterpart to the radio source. The ATCA synthesized beam is shown in the bottom right-hand corner of each panel.

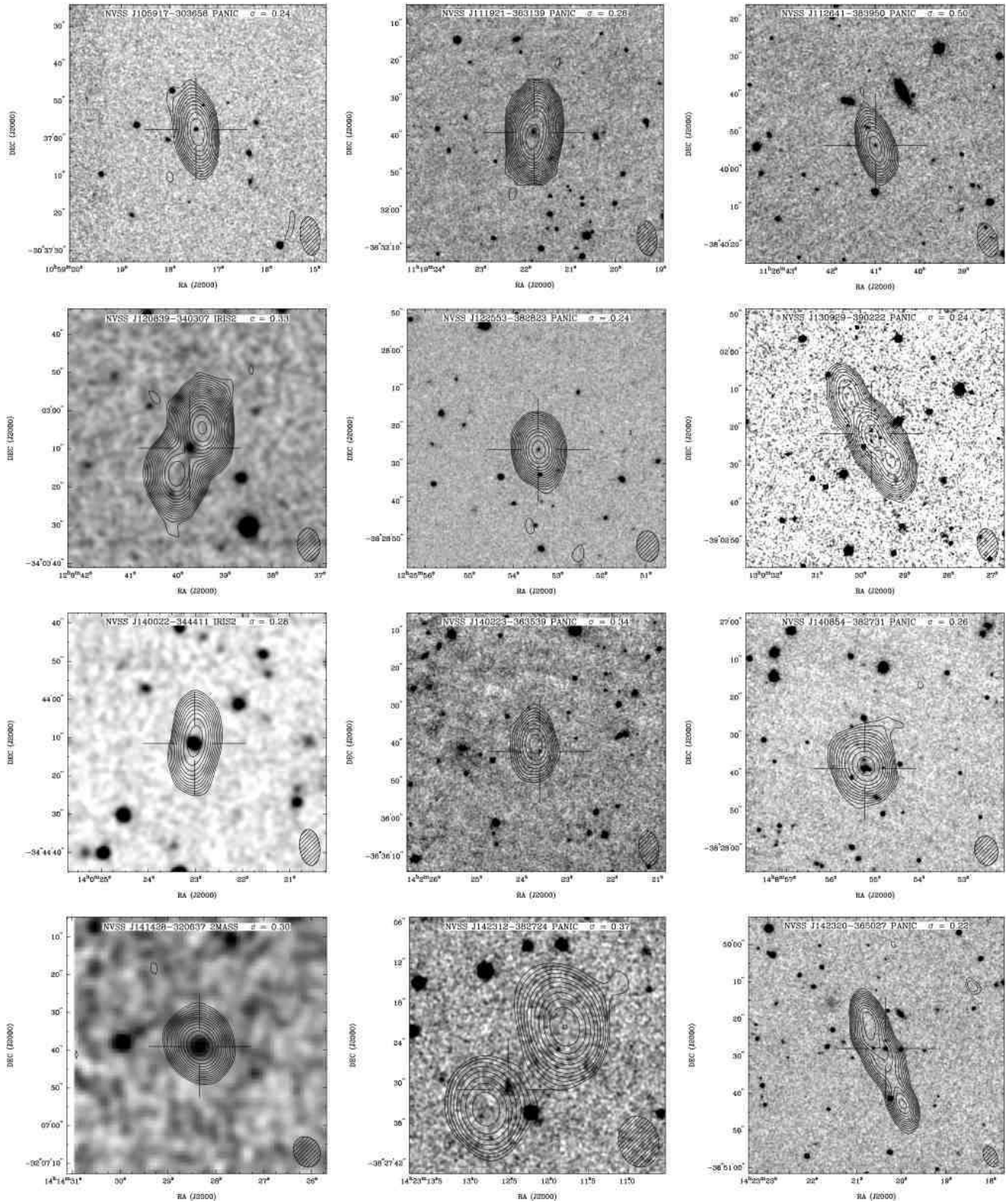

Figure 2. *continued.*

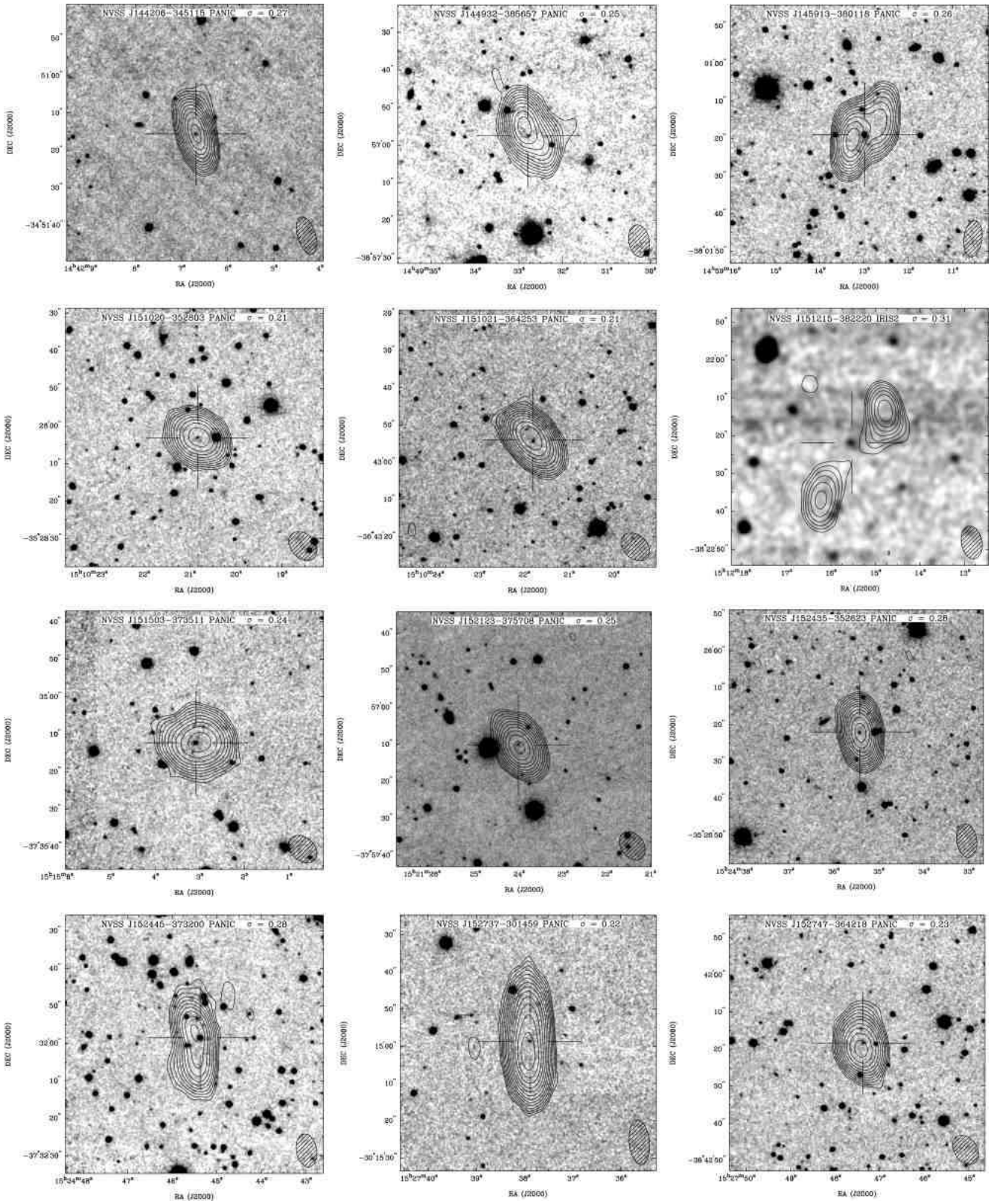

Figure 2. *continued.*

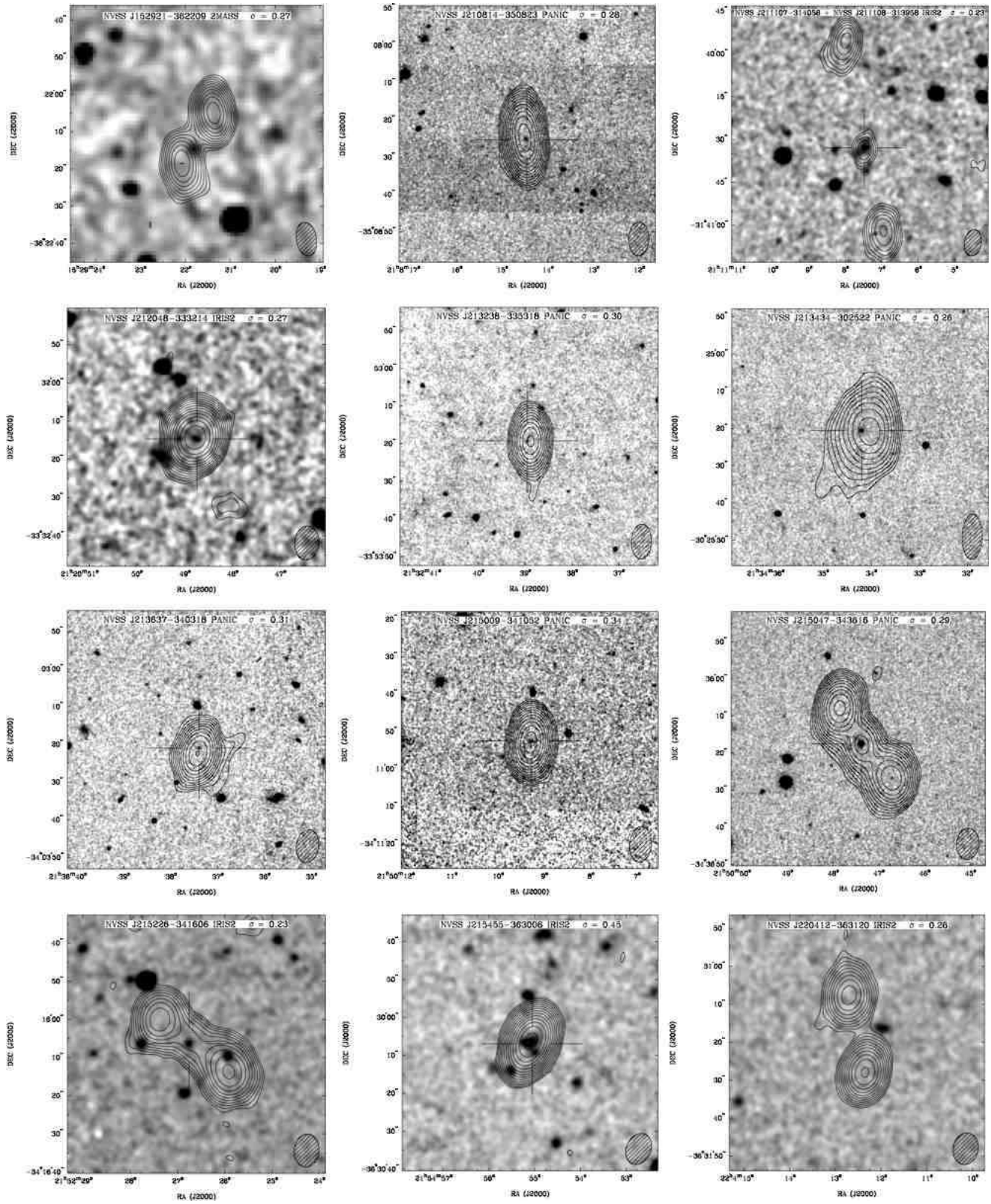

Figure 2. *continued.*

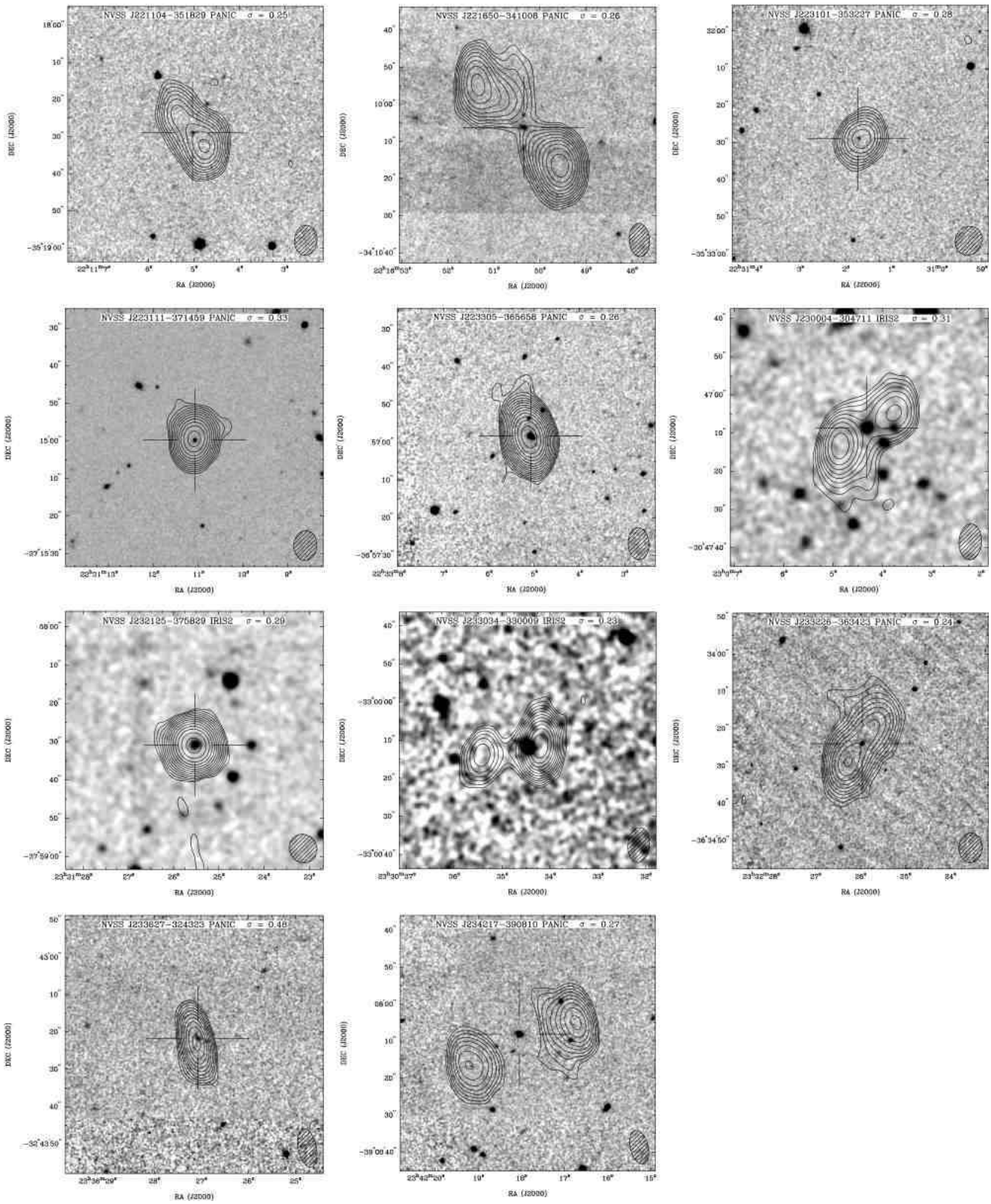

Figure 2. *continued.*

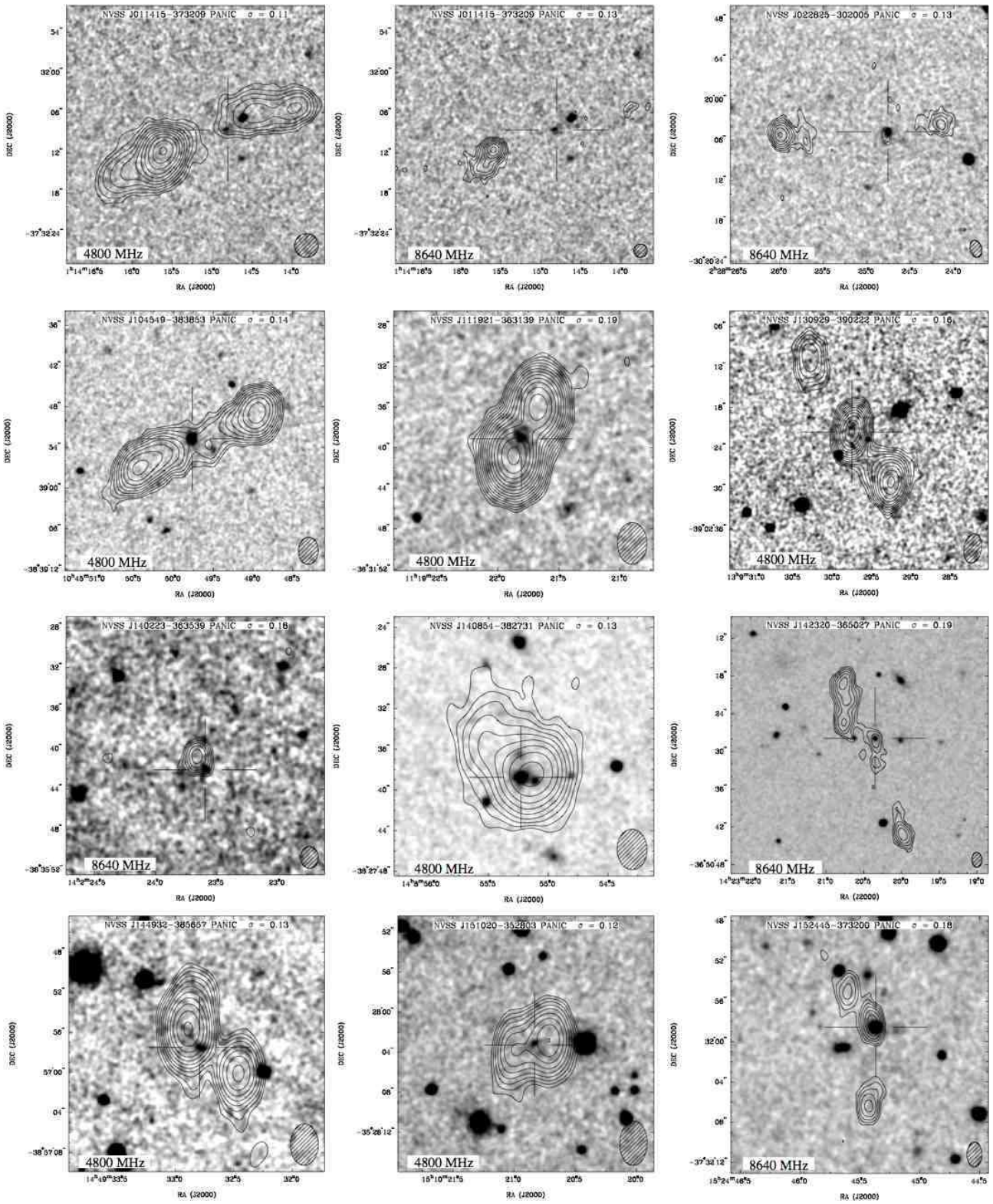

Figure 3. 4800 or 8640-MHz ATCA contours overlaid on the K-band images including some of the sources which had uncertain identifications at 2368 MHz. These are discussed in Section 3.2. The K-band images show which instrument they are from, in the header, and they have been smoothed using a gaussian kernel of 3 pixels FWHM. All the radio contours are from natural-weighted images with the lowest contour at 3 sigma, and the contours are a geometric progression in $\sqrt{2}$. The rms noise (σ) is shown in the header of each image in mJy beam^{-1}. Crosshairs mark the K-band counterpart to the radio source. The ATCA synthesized beam is shown in the bottom right-hand corner of each panel.

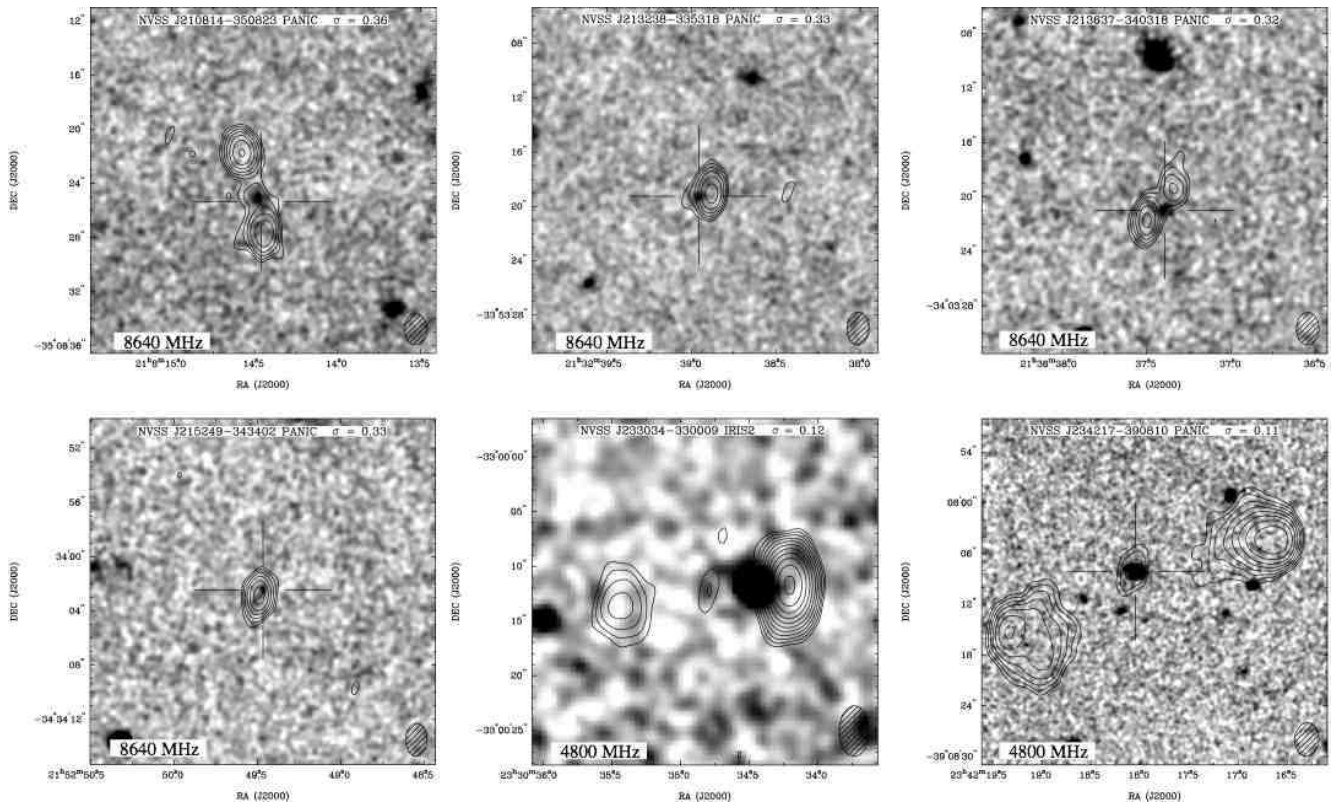

Figure 3. *continued.*

to sources from De Breuck et al. (2004) and 'SC' is written for sources without K, which were identified on the SuperCOSMOS UKJ and UKR fields. Two objects are from the 2MASS catalogue.

(8) Spectral index from the 5-point fit from Paper I. Some sources have spectral shapes that could not be fitted with a 5-point linear or quadratic fit and the spectral index between 843 and 1400 MHz is shown instead. For the sources from De Breuck et al. (2004), the spectral index has been recalculated using updated flux densities from the latest SUMSS catalogue release (version 2.1). Sources with flattening radio spectra at high frequencies (marked *f*) have a spectral index fitted at 1400MHz (see Paper I). The spectral indices from Klamer et al. (2006), used for the sources marked *g*, are the result of fits to flux densities at up to seven frequencies between 0.843–18 GHz.

(9) Largest angular size (LAS) from the natural-weighted 2368-MHz images in Paper I, given in arcsec. The sources which are also in the SUMSS–NVSS sample have LAS values from De Breuck et al. (2004) or Klamer et al. (2006) and are not all measured at 2368 MHz. The LAS values for NVSS J002431−303330 and NVSS J103615−321659 have been updated since Paper I, with corresponding new position angles of 19 and 17 degrees respectively.

Table 2 includes all the sources that meet our selection criteria from Paper I (tables 1 and 3), and that have K-band magnitudes available from our observations, 2MASS, or De Breuck et al. (2004). NVSS J230527−360534 and NVSS J231727−352606 are in both the SUMSS–NVSS and our MRCR–SUMSS samples and have K-band magnitude limits listed in De Breuck et al. (2004), but were reobserved to refine the magnitude; our new magnitude is shown in the table. The combined source NVSS J023601−314204/J023605−314235 and NVSS J103441−394957 have red identifications in SuperCOSMOS and were retained in the sample because the counterpart was not located until we had high-resolution ATCA images. These sources have followup spectroscopy presented in Paper III.

Of the 175 sources with K-band and/or spectroscopic (see Paper III) followup, 93 per cent (162) had clear K-band counterparts to the radio images, two had SuperCOSMOS identifications and 11 had counterparts too faint to detect or measure.

3.1 4800- and 8640-MHz flux densities

The results of the 4800- and 8640-MHz observations of 29 sources from the MRCR–SUMSS sample are given in Table 3. The columns are the following:

(1) Name of the source in the NVSS catalogue in IAU J2000 format.
(2) The 4800- and 8640-MHz integrated flux densities. In most cases, these were obtained using the MIRIAD Gaussian fitting task IMFIT. However, when there was a significant amount of diffuse extended emission, the flux densities were calculated by summing the pixel values in a box or polygon and correcting for the background level. The typical flux density uncertainties are ∼4 per cent at 4800 MHz and ∼10 per cent at 8640 MHz, though in a few cases the 8640 MHz flux densities are uncertain by up to ∼20 per cent due to

Table 2. K-band photometry results. Details of each column are given in Section 3.

(1) Name	(2) K (4″ ap.) (mag)	(3) K (8″ ap.) (mag)	(4) $\mathrm{RA}^{K-\mathrm{band}}_{\mathrm{J2000}}$ (h m s)	(5) $\mathrm{DEC}^{K-\mathrm{band}}_{\mathrm{J2000}}$ ($^\circ$ ′ ″)	(6) K int. time (min)	(7) Origin of K imaging	(8) $\alpha_{(5-\mathrm{point\ fit})}$	(9) LAS_{2368} (arcsec)
NVSS J000231−342614	18.2 ± 0.2	17.9 ± 0.2	00:02:31.50	−34:26:16.1	15	IRIS2	-1.07 ± 0.05	55.0
NVSS J000640−345027	19.4 ± 0.1	19.3 ± 0.4	00:06:40.81	−34:50:27.1	9	PANIC	-0.82 ± 0.05	1.7
NVSS J000717−365557	18.9 ± 0.2	19.1 ± 0.3	00:07:17.30	−36:55:56.2	9	PANIC	-0.94 ± 0.05	8.7
NVSS J000742−304325	18.9 ± 0.1	18.6 ± 0.2	00:07:42.83	−30:43:24.2	9	PANIC	-1.16 ± 0.05	< 2
NVSS J001210−342103	> 20.0	—	—	—	9	PANIC	-1.08 ± 0.05	36.6
NVSS J001215−374113	20.7 ± 0.2	19.8 ± 0.5	00:12:15.85	−37:41:13.5	18	PANIC	-1.30 ± 0.04	< 2
NVSS J001506−330155	17.6 ± 0.2	17.1 ± 0.2	00:15:06.31	−33:01:54.0	15	IRIS2	-1.00 ± 0.05	16.4
NVSS J002037−355717	19.4 ± 0.2	19.2 ± 0.4	00:20:37.66	−35:57:19.1	9	PANIC	-1.10 ± 0.04	16.2
NVSS J002431−303330	18.8 ± 0.1	18.7 ± 0.1	00:24:31.80	−30:33:28.1	15	IRIS2	-0.87^{f}	7.7
NVSS J002805−362049	18.7 ± 0.3	18.5 ± 0.3	00:28:05.83	−36:20:50.2	15	IRIS2	-0.98 ± 0.05	25.9
NVSS J002913−353637	18.1 ± 0.1	17.5 ± 0.1	00:29:13.55	−35:36:39.4	15	IRIS2	-0.92 ± 0.05	7.7
NVSS J002915−304034	18.4 ± 0.1	18.6 ± 0.3	00:29:15.30	−30:40:35.4	9	PANIC	-0.70 ± 0.10^{j}	23.9
NVSS J003445−372348	17.0 ± 0.1	16.4 ± 0.1	00:34:45.66	−37:23:47.4	15	IRIS2	-1.18 ± 0.04	32.7
NVSS J003758−340630	17.7 ± 0.1	17.2 ± 0.1	00:37:58.51	−34:06:30.8	15	IRIS2	-1.08 ± 0.04	19.4
NVSS J004000−303333	19.5 ± 0.2	19.8 ± 0.4	00:40:00.01	−30:33:32.7	18	PANIC	-1.17 ± 0.05	7.2
NVSS J004030−304753	18.8 ± 0.2	19.0 ± 0.4	00:40:30.68	−30:47:55.7	9	PANIC	-1.26 ± 0.06	24.5
NVSS J004136−345046	19.2 ± 0.3	19.1 ± 0.6	00:41:36.22	−34:50:46.8	9	PANIC	-1.11 ± 0.05	7.9
NVSS J004147−303658	19.6 ± 0.3	17.7 ± 0.3	00:41:47.59	−30:36:56.1	5	PANIC	-0.95 ± 0.05	15.8
NVSS J004230−343733	17.0 ± 0.1	16.9 ± 0.1	00:42:30.38	−34:37:33.2	9	PANIC	-1.02 ± 0.05	31.3
NVSS J004609−341049	17.1 ± 0.1	17.2 ± 0.1	00:46:09.40	−34:10:49.4	9	PANIC	-0.91 ± 0.05	29.2
NVSS J005320−322756	> 20.4	—	—	—	15	PANIC	-1.08 ± 0.05	11.8
NVSS J005402−361929	20.6 ± 0.5	—	00:54:02.56	−36:19:30.5	18	PANIC	-1.14 ± 0.05	2.9
NVSS J005509−361736	20.6 ± 0.5	—	00:55:09.74	−36:17:36.4	27	PANIC	-0.81 ± 0.08^{j}	2.8
NVSS J005716−373238	17.8 ± 0.1	17.5 ± 0.1	00:57:16.54	−37:32:41.6	9	PANIC	-1.26 ± 0.05	11.7
NVSS J010021−394347	18.1 ± 0.1	18.4 ± 0.3	01:00:21.18	−39:43:46.2	9	PANIC	-0.91 ± 0.05	6.1
NVSS J010942−341154	18.7 ± 0.2	18.1 ± 0.2	01:09:42.46	−34:11:54.5	9	PANIC	-1.14 ± 0.05	< 2
NVSS J011415−373209	19.1 ± 0.2	17.9 ± 0.1	01:14:14.81	−37:32:08.6	9	PANIC	-1.25 ± 0.04	17.1
NVSS J011606−331241[i]	18.6 ± 0.2	18.1 ± 0.2	01:16:06.77	−33:12:42.8		DB	-1.26^{f}	6.4
NVSS J011745−352644	18.6 ± 0.1	16.6 ± 0.1	01:17:45.82	−35:26:44.5	9	PANIC	-0.94 ± 0.05	4.6
NVSS J012754−372236	18.5 ± 0.2	18.2 ± 0.3	01:27:54.94	−37:22:34.6	3	PANIC	-1.26 ± 0.05	4.9
NVSS J012932−385433	18.5 ± 0.1	18.3 ± 0.2	01:29:32.92	−38:54:34.5	9	PANIC	-1.02 ± 0.05	1.4
NVSS J013314−304401	20.1 ± 0.5	—	01:33:14.99	−30:44:02.4	9	PANIC	-1.09 ± 0.06	< 2
NVSS J013537−364411	18.5 ± 0.1	17.7 ± 0.1	01:35:37.73	−36:44:11.8	9	PANIC	-1.35 ± 0.04	4.1
NVSS J013554−332513	20.4 ± 0.6	—	01:35:54.02	−33:25:14.8	9	PANIC	-1.09 ± 0.04	11.9
NVSS J014445−361945	18.8 ± 0.5	19.3 ± 0.6	01:44:45.40	−36:19:45.2	6	PANIC	-1.19 ± 0.05	7.0
NVSS J014813−384340	18.4 ± 0.1	18.8 ± 0.3	01:48:13.72	−38:43:41.7	9	PANIC	-1.20 ± 0.05	4.3
NVSS J020201−374750	19.3 ± 0.2	18.9 ± 0.3	02:02:01.57	−37:47:50.1	18	PANIC	-1.15 ± 0.05	17.3
NVSS J021208−343111	19.0 ± 0.2	18.7 ± 0.3	02:12:08.67	−34:31:11.3	9	PANIC	-1.06 ± 0.05	7.0
NVSS J021759−301512	18.3 ± 0.1	18.2 ± 0.2	02:17:59.80	−30:15:12.8	9	PANIC	-1.04 ± 0.05	11.7
NVSS J022825−302005	18.3 ± 0.1	18.2 ± 0.2	02:28:24.76	−30:20:04.8	9	PANIC	-1.03 ± 0.05	19.5
NVSS J023601−314204[a]	SC	—	02:36:04.04	−31:42:23.4[b]		SC	-0.35 ± 0.09^{j}	58.8
NVSS J023605−314235[a]								
NVSS J024523−325626	19.6 ± 0.3	19.5 ± 0.5	02:45:23.83	−32:56:26.2	9	PANIC	-0.66 ± 0.09^{j}	< 2
NVSS J024811−335106	18.7 ± 0.2	19.7 ± 0.6	02:48:11.96	−33:51:02.6	9	PANIC	-0.80 ± 0.05	33.2
NVSS J025737−310104	19.5 ± 0.2	—	02:57:37.81	−31:01:04.3	9	PANIC	-0.99 ± 0.05	4.4
NVSS J030026−322103	17.4 ± 0.1	17.4 ± 0.1	03:00:26.06	−32:21:01.5	9	PANIC	-0.97 ± 0.05	7.0
NVSS J030037−310337	18.2 ± 0.1	18.0 ± 0.1	03:00:37.54	−31:03:49.2	9	PANIC	-1.04 ± 0.07	72.1
NVSS J030431−315308	18.7 ± 0.2	19.0 ± 0.3	03:04:31.91	−31:53:08.4	9	PANIC	-1.18 ± 0.05	2.4
NVSS J031902−322319	19.2 ± 0.2	—	03:19:02.10	−32:23:20.1	9	PANIC	-0.70 ± 0.09^{j}	5.6
NVSS J032558−320154	> 19.9	—	—	—	9	PANIC	-1.34 ± 0.05	26.4
NVSS J034027−331711	19.4 ± 0.2	18.7 ± 0.3	03:40:27.22	−33:17:11.1	9	PANIC	-0.96 ± 0.05	22.9
NVSS J100129−364834	17.9 ± 0.1	18.0 ± 0.1	10:01:28.98	−36:48:34.0	15	IRIS2	-1.16 ± 0.06	13.2
NVSS J101008−383629	18.9 ± 0.2	—	10:10:08.02	−38:36:29.2	9	PANIC	-1.07 ± 0.04	10.7
NVSS J101545−385816	18.2 ± 0.2	17.9 ± 0.2	10:15:45.85	−38:58:17.0	9	PANIC	-1.13 ± 0.05	9.4
NVSS J101730−384643	18.0 ± 0.2	18.0 ± 0.2	10:17:30.50	−38:46:43.8	9	PANIC	-1.28 ± 0.05	< 2
NVSS J102024−342257	18.7 ± 0.2	18.7 ± 0.3	10:20:24.44	−34:22:57.3	9	PANIC	-1.13 ± 0.05	5.5
NVSS J103441−394957	SC	—	10:34:42.06	−39:49:58.0[b]		SC	-1.05 ± 0.05	29.0
NVSS J103615−321659	19.3 ± 0.2	—	10:36:15.26	−32:16:57.4	9	PANIC	-1.22 ± 0.05	10.4
NVSS J103626−375819	18.7 ± 0.2	18.5 ± 0.2	10:36:25.79	−37:58:19.2	9	PANIC	-1.17 ± 0.05	13.1
NVSS J104549−383853	17.3 ± 0.2	17.3 ± 0.2	10:45:49.76	−38:38:52.9	9	PANIC	-0.91 ± 0.04	16.1
NVSS J105917−303658	18.8 ± 0.1	—	10:59:17.45	−30:36:57.5	9	PANIC	-1.22 ± 0.05	2.2
NVSS J110350−352643	19.0 ± 0.2	18.6 ± 0.2	11:03:50.64	−35:26:43.2	15	IRIS2	-1.21 ± 0.04	1.6
NVSS J110753−394520	18.5 ± 0.1	18.6 ± 0.2	11:07:53.64	−39:45:21.0	9	PANIC	-0.91 ± 0.10^{j}	6.6
NVSS J110822−390601	> 19.8	—	—	—	9	PANIC	-1.15 ± 0.05	3.4
NVSS J111026−384544	17.4 ± 0.1	17.2 ± 0.1	11:10:26.40	−38:45:43.6	9	PANIC	-1.01 ± 0.04	2.3
NVSS J111546−391410	16.4 ± 0.2	16.4 ± 0.2	11:15:46.47	−39:14:10.2	9	PANIC	-1.08 ± 0.04	20.2
NVSS J111921−363139	18.7 ± 0.1	19.1 ± 0.2	11:19:21.81	−36:31:39.1	45	PANIC	-1.41 ± 0.04	< 2
NVSS J112641−383950	20.3 ± 0.3	—	11:26:41.00	−38:39:53.5	36	PANIC	-1.25 ± 0.04	< 2
NVSS J112920−314619	20.5 ± 0.6	19.9 ± 0.7	11:29:20.70	−31:46:21.1	9	PANIC	-0.79 ± 0.11^{j}	17.3
NVSS J113002−384532	19.3 ± 0.1	19.4 ± 0.2	11:30:02.79	−38:45:35.2	45	PANIC	-1.20 ± 0.05	< 2

Table 2. K-band photometry results *continued*

(1) Name	(2) K (4″ ap.) (mag)	(3) K (8″ ap.) (mag)	(4) $\mathrm{RA}^{K-\mathrm{band}}_{\mathrm{J2000}}$ (h m s)	(5) $\mathrm{DEC}^{K-\mathrm{band}}_{\mathrm{J2000}}$ ($^\circ$ ′ ″)	(6) K int. time (min)	(7) Origin of K imaging	(8) $\alpha_{(5-\mathrm{point\ fit})}$	(9) LAS_{2368} (arcsec)
NVSS J113801−392257	18.8 ± 0.2	18.9 ± 0.3	11:38:01.26	−39:23:02.3	9	PANIC	-1.08 ± 0.04	20.1
NVSS J115829−374410	21.4 ± 0.7	—	11:58:29.32	−37:44:10.8	54	PANIC	-1.32 ± 0.05	1.2
NVSS J115853−382921	18.2 ± 0.3	18.4 ± 0.3	11:58:53.45	−38:29:21.5	9	PANIC	-1.29 ± 0.04	1.1
NVSS J120839−340307	18.0 ± 0.1	17.7 ± 0.1	12:08:39.75	−34:03:09.6	15	IRIS2	-1.20 ± 0.04	13.5
NVSS J122553−382823	19.2 ± 0.2	—	12:25:53.43	−38:28:26.2	9	PANIC	-1.26 ± 0.04	1.4
NVSS J123602−364522	18.5 ± 0.2	18.4 ± 0.2	12:36:02.15	−36:45:21.6	15	IRIS2	-1.22 ± 0.05	14.7
NVSS J125448−391358	18.9 ± 0.3	18.7 ± 0.3	12:54:48.83	−39:13:57.9	15	IRIS2	-1.15 ± 0.05	< 2
NVSS J130929−390222	19.6 ± 0.2	18.5 ± 0.2	13:09:29.75	−39:02:21.6	9	PANIC	-1.06 ± 0.04	20.9
NVSS J131102−372516	18.6 ± 0.2	18.1 ± 0.2	13:11:02.41	−37:25:16.8	15	IRIS2	-1.14 ± 0.04	2.8
NVSS J131202−394600	17.0 ± 0.1	17.0 ± 0.1	13:12:02.58	−39:45:56.6	9	PANIC	-0.79 ± 0.05	16.0
NVSS J132551−344606	17.3 ± 0.1	16.9 ± 0.1	13:25:51.96	−34:46:07.5	15	IRIS2	-0.55 ± 0.09[j]	6.6
NVSS J134143−370612	19.0 ± 0.2	18.6 ± 0.2	13:41:43.37	−37:06:12.2	15	IRIS2	-1.14 ± 0.05	2.7
NVSS J140010−374240	17.0 ± 0.1	17.0 ± 0.1	14:00:10.58	−37:42:40.1	9	PANIC	-0.86 ± 0.05	10.3
NVSS J140022−344411	16.3 ± 0.2	16.2 ± 0.2	14:00:23.01	−34:44:11.3	15	IRIS2	-1.02 ± 0.05	8.6
NVSS J140037−354439	18.5 ± 0.1	18.1 ± 0.2	14:00:37.76	−35:44:40.8	9	PANIC	-1.36 ± 0.09[j]	2.4
NVSS J140223−363539	19.8 ± 0.3	19.9 ± 0.6	14:02:23.63	−36:35:42.2	27	PANIC	-1.38 ± 0.05	3.8
NVSS J140303−384625	19.3 ± 0.2	—	14:03:03.92	−38:46:23.4	9	PANIC	-1.02 ± 0.05	18.5
NVSS J140854−382731	16.9 ± 0.2	16.6 ± 0.2	14:08:55.24	−38:27:38.7	9	PANIC	-1.28 ± 0.05	5.3
NVSS J141428−320637	15.5 ± 0.2	15.5 ± 0.2	14:14:28.27	−32:06:38.7[c]		2MASS	-1.27 ± 0.05	1.6
NVSS J142013−384113	18.8 ± 0.2	18.7 ± 0.2	14:20:13.85	−38:41:13.2	15	IRIS2	-1.19 ± 0.05	17.2
NVSS J142312−382724	18.8 ± 0.2	18.8 ± 0.2	14:23:12.53	−38:27:31.0	9	PANIC	-1.03 ± 0.05	16.9
NVSS J142320−365027	18.3 ± 0.1	17.7 ± 0.1	14:23:20.34	−36:50:28.0	9	PANIC	-0.93 ± 0.05	18.5
NVSS J143122−353300	20.0 ± 0.4	—	14:31:22.71	−35:32:55.7	9	PANIC	-1.18 ± 0.05	16.0
NVSS J143806−395307	19.2 ± 0.5	18.6 ± 0.5	14:38:06.28	−39:53:09.4	15	IRIS2	-1.08 ± 0.05	3.0
NVSS J144206−345115	> 20.1	—	14:42:06.69	−34:51:15.6	18	PANIC	-0.94 ± 0.05	2.5
NVSS J144245−373827	17.8 ± 0.1	17.5 ± 0.1	14:42:45.49	−37:38:29.4	9	PANIC	-1.09 ± 0.04	16.4
NVSS J144932−385657	19.8 ± 0.2	—	14:49:32.79	−38:56:57.5	45	PANIC	-1.23 ± 0.09[j]	7.5
NVSS J145045−380012	16.6 ± 0.1	16.4 ± 0.1	14:50:45.04	−38:00:13.3	9	PANIC	-0.94 ± 0.05	10.2
NVSS J145133−350202	19.6 ± 0.2	20.0 ± 0.7	14:51:33.18	−35:02:03.3	27	PANIC	-0.76 ± 0.05	1.0
NVSS J145312−355542	17.7 ± 0.1	17.3 ± 0.1	14:53:12.56	−35:55:42.9	9	PANIC	-0.99 ± 0.05	9.1
NVSS J145403−370423	19.5 ± 0.2	—	14:54:03.40	−37:04:26.3	9	PANIC	-1.25 ± 0.06	14.8
NVSS J145603−370142	18.0 ± 0.3	18.0 ± 0.3	14:56:03.52	−37:01:46.9	15	IRIS2	-1.22 ± 0.05	24.2
NVSS J145913−380118	18.3 ± 0.1	18.2 ± 0.2	14:59:12.99	−38:01:19.0	9	PANIC	-1.12 ± 0.05	8.3
NVSS J150026−393951	16.8 ± 0.1	16.5 ± 0.1	15:00:26.29	−39:39:51.9	15	IRIS2	-1.36 ± 0.04	18.1
NVSS J150405−394733	18.3 ± 0.2	17.6 ± 0.2	15:04:05.55	−39:47:36.9	9	PANIC	-1.02[f]	20.7
NVSS J151020−352803	20.2 ± 0.2	20.5 ± 0.6	15:10:20.84	−35:28:03.2	45	PANIC	-1.35 ± 0.05	4.2
NVSS J151021−364253	20.1 ± 0.2	—	15:10:21.80	−36:42:54.1	45	PANIC	-1.09 ± 0.05	6.0
NVSS J151215−382220	17.2 ± 0.1	16.9 ± 0.1	15:12:15.51	−38:22:21.7	15	IRIS2	-1.14 ± 0.06	28.1
NVSS J151503−373511	17.3 ± 0.1	17.1 ± 0.1	15:15:03.09	−37:35:12.2	9	PANIC	-1.49 ± 0.05	7.8
NVSS J151610−342718	18.0 ± 0.3	17.9 ± 0.3	15:16:10.45	−34:27:18.5	9	PANIC	-1.15 ± 0.05	11.5
NVSS J152123−375708	19.3 ± 0.3	19.4 ± 0.6	15:21:24.02	−37:57:10.2	27	PANIC	-0.89 ± 0.05	3.6
NVSS J152149−390517	18.6 ± 0.1	18.4 ± 0.1	15:21:49.13	−39:05:20.5	15	IRIS2	-1.37 ± 0.04	11.6
NVSS J152435−352623	20.9 ± 0.5	—	15:24:35.41	−35:26:22.0	36	PANIC	-1.17 ± 0.05	< 2
NVSS J152445−373200	18.3 ± 0.1	18.6 ± 0.2	15:24:45.37	−37:31:58.5	9	PANIC	-1.07 ± 0.05	13.5
NVSS J152737−301459	17.6 ± 0.2	—	15:27:37.88	−30:14:58.6	9	PANIC	-1.30 ± 0.04	13.3
NVSS J152747−364218	19.6 ± 0.2[d]	18.6 ± 0.2	15:27:47.38	−36:42:18.4	27	PANIC	-1.12 ± 0.04	< 2
NVSS J152921−362209	15.7 ± 0.3[d,e]	15.7 ± 0.3	15:29:21.77	−36:22:14.6[c]		2MASS	-1.16 ± 0.05	16.0
NVSS J153757−362659	18.9 ± 0.3	—	15:37:57.23	−36:26:58.2	15	IRIS2	-1.01 ± 0.05	24.0
NVSS J154513−344834	> 20.8	—	15:45:13.74	−34:48:34.3	9	PANIC	-1.10 ± 0.04	1.3
NVSS J201943−364542	18.4 ± 0.3	18.3 ± 0.3	20:19:43.54	−36:45:43.2	15	IRIS2	-1.17 ± 0.05	14.7
NVSS J202720−341150	> 20.3	—	20:27:21.00	−34:11:52.0	18	PANIC	-1.12 ± 0.04	22.9
NVSS J202856−353709[i]	16.9 ± 0.1[d]	16.6 ± 0.1	20:28:56.77	−35:37:06.0		DB	-1.36 ± 0.10[j]	35.8
NVSS J202942−341300	19.3 ± 0.2	—	20:29:42.21	−34:13:01.3	9	PANIC	-1.20 ± 0.05	5.9
NVSS J202945−344812[i]	17.6 ± 0.1	17.3 ± 0.1	20:29:45.82	−34:48:15.5		DB	-0.94[g]	18.9
NVSS J204526−371625	> 20.1	—	—	—	18	PANIC	-1.11 ± 0.05	2.2
NVSS J204601−335656	19.7 ± 0.4	18.5 ± 0.4	20:46:01.09	−33:56:57.1	9	PANIC	-1.13 ± 0.05	2.2
NVSS J204859−393404	18.9 ± 0.1	18.0 ± 0.1	20:48:59.01	−39:34:04.2	9	PANIC	-1.40 ± 0.05	8.2
NVSS J210626−314003	18.7 ± 0.2	18.8 ± 0.4	21:06:25.90	−31:40:01.5	9	PANIC	-1.04 ± 0.05	24.2
NVSS J210814−350823	19.5 ± 0.5	—	21:08:14.46	−35:08:25.3	9	PANIC	-1.08 ± 0.04	8.1
NVSS J211107−314058[a] NVSS J211108−313958	18.3 ± 0.2	17.5 ± 0.2	21:11:07.50	−31:40:32.7	15	IRIS2	-1.26 ± 0.07	67.8
NVSS J212048−333214	19.1 ± 0.1	18.6 ± 0.1	21:20:48.76	−33:32:14.4	15	IRIS2	-1.07 ± 0.04	4.5
NVSS J212706−340322	18.1 ± 0.2	18.2 ± 0.2	21:27:06.05	−34:03:27.1	9	PANIC	-0.90 ± 0.05	23.1
NVSS J212803−313912	> 18.5	—	—	—	15	IRIS2	-1.12 ± 0.05	38.3
NVSS J213238−335318	19.8 ± 0.4	—	21:32:38.95	−33:53:18.9	9	PANIC	-1.43 ± 0.05	< 2
NVSS J213434−302522	16.8 ± 0.2	16.7 ± 0.2	21:34:34.20	−30:25:20.6	9	PANIC	-1.12 ± 0.05	8.1
NVSS J213637−340318	19.7 ± 0.2	19.6 ± 0.3	21:36:37.39	−34:03:21.1	36	PANIC	-1.36 ± 0.05	3.6
NVSS J214114−332307	19.1 ± 0.3	19.6 ± 0.3	21:41:14.04	−33:23:09.4	15	IRIS2	-1.21 ± 0.04	38.6
NVSS J215009−341052	19.6 ± 0.3	—	21:50:09.30	−34:10:52.4	18	PANIC	-1.18 ± 0.05	1.7

Table 2. K-band photometry results *continued*

(1) Name	(2) K (4″ ap.) (mag)	(3) K (8″ ap.) (mag)	(4) $\mathrm{RA}^{K-\mathrm{band}}_{\mathrm{J2000}}$ (h m s)	(5) $\mathrm{DEC}^{K-\mathrm{band}}_{\mathrm{J2000}}$ (° ′ ″)	(6) K int. time (min)	(7) Origin of K imaging	(8) $\alpha_{(5-\mathrm{point\ fit})}$	(9) LAS_{2368} (arcsec)
NVSS J215047−343616	17.4 ± 0.1	17.0 ± 0.1	21:50:47.38	−34:36:17.5	9	PANIC	-1.00 ± 0.05	23.4
NVSS J215226−341606	18.3 ± 0.3	18.0 ± 0.3	21:52:26.74	−34:16:06.2	15	IRIS2	-0.95 ± 0.05	21.4
NVSS J215249−343402	> 20.0	—	21:52:49.47	−34:34:02.6	9	PANIC	-1.46 ± 0.05	< 2
NVSS J215455−363006	17.7 ± 0.1	16.9 ± 0.1	21:54:55.08	−36:30:06.8	15	IRIS2	-1.17 ± 0.04	5.2
NVSS J215717−313449	> 20.2	—	—	—	18	PANIC	-0.36 ± 0.10^{j}	9.7
NVSS J220412−363120	> 19.6	17.6 ± 0.1	—	—	15	IRIS2	-1.18 ± 0.05	20.7
NVSS J221104−351829	19.0 ± 0.2	19.1 ± 0.5	22:11:05.04	−35:18:28.8	9	PANIC	-1.12 ± 0.05	9.4
NVSS J221542−361311	18.6 ± 0.1	19.1 ± 0.4	22:15:42.98	−36:13:14.3	9	PANIC	-0.82 ± 0.05	12.2
NVSS J221650−341008	16.4 ± 0.3	16.2 ± 0.3	22:16:50.34	−34:10:06.1	9	PANIC	-1.04 ± 0.04	29.5
NVSS J221940−350100	18.5 ± 0.3	18.1 ± 0.3	22:19:40.22	−35:01:02.1	15	IRIS2	-0.94 ± 0.05	4.1
NVSS J223101−353227	19.5 ± 0.2	19.6 ± 0.6	22:31:01.72	−35:32:28.8	9	PANIC	-1.83 ± 0.05	2.7
NVSS J223111−371459	17.6 ± 0.1	17.3 ± 0.1	22:31:11.09	−37:14:59.9	9	PANIC	-1.01 ± 0.05	2.4
NVSS J223305−365658	16.6 ± 0.1	16.3 ± 0.1	22:33:05.08	−36:56:58.2	9	PANIC	-0.90 ± 0.04	4.4
NVSS J223953−344433	19.6 ± 0.3	19.4 ± 0.5	22:39:53.99	−34:44:37.2	18	PANIC	-1.20 ± 0.06	25.1
NVSS J225225−344144	19.1 ± 0.3	18.7 ± 0.4	22:52:25.15	−34:41:43.6	9	PANIC	-0.65 ± 0.10^{j}	8.0
NVSS J225719−343954[i]	16.7 ± 0.1	16.5 ± 0.1	22:57:19.63	−34:39:54.6		DB	-1.77^{g}	< 6
NVSS J230004−304711	17.4 ± 0.1	17.0 ± 0.1	23:00:04.31	−30:47:08.7	15	IRIS2	-0.80 ± 0.05	15.3
NVSS J230226−364744	18.7 ± 0.2	18.7 ± 0.2	23:02:26.62	−36:47:45.7	18	PANIC	-0.80 ± 0.12^{j}	< 2
NVSS J230527−360534[h]	> 21.2	—	—	—	99	PANIC	-1.39^{g}	< 1
NVSS J230846−334810[i]	17.0 ± 0.1	16.6 ± 0.1	23:08:46.73	−33:48:12.4		DB	-1.26 ± 0.10^{j}	29.8
NVSS J231723−371934	19.5 ± 0.2	19.8 ± 0.6	23:17:23.70	−37:19:32.1	9	PANIC	-1.12 ± 0.05	16.4
NVSS J231727−352606[h]	> 20.7	—	—	—	9	PANIC	-1.28 ± 0.05	4.0
NVSS J232007−302127	> 19.0	—	—	—	6	PANIC	-1.26 ± 0.04	6.3
NVSS J232058−365157[i]	18.6 ± 0.2	18.7 ± 0.4	23:20:58.28	−36:51:59.7		DB	-0.97^{g}	< 5
NVSS J232125−375829	17.9 ± 0.1	17.9 ± 0.1	23:21:25.55	−37:58:30.7	15	IRIS2	-1.01 ± 0.04	< 2
NVSS J233034−330009	17.2 ± 0.3	17.1 ± 0.3	23:30:34.49	$-33{:}00{:}11.5^{k}$	15	IRIS2	-1.18 ± 0.05	15.3
NVSS J233226−363423	17.9 ± 0.1	18.0 ± 0.1	23:32:25.96	−36:34:24.1	9	PANIC	-1.06 ± 0.05	10.6
NVSS J233535−343330	18.9 ± 0.2	18.6 ± 0.2	23:35:35.51	−34:33:32.4	15	IRIS2	-1.08 ± 0.04	6.8
NVSS J233627−324323	18.5 ± 0.1	18.2 ± 0.2	23:36:27.09	−32:43:21.8	9	PANIC	-1.46 ± 0.05	< 2
NVSS J233729−355529[i]	19.2 ± 0.3	17.9 ± 0.2	23:37:29.76	−35:55:29.0		DB	-1.53 ± 0.09^{j}	7.4
NVSS J234145−350624[i]	16.9 ± 0.1	16.3 ± 0.1	23:41:45.85	−35:06:22.2		DB	-1.11^{g}	< 5
NVSS J234217−390810	17.4 ± 0.1	17.3 ± 0.1	23:42:18.05	−39:08:08.0	8	PANIC	-1.01 ± 0.05	29.2
NVSS J234235−384526	19.0 ± 0.1	18.8 ± 0.2	23:42:35.04	−38:45:25.0	9	PANIC	-1.36 ± 0.05	9.4
NVSS J235148−385546	19.1 ± 0.2	19.4 ± 0.5	23:51:48.33	−38:55:46.9	9	PANIC	-1.19^{f}	6.8
NVSS J235638−390923	18.8 ± 0.1	18.9 ± 0.3	23:56:38.66	−39:09:25.0	9	PANIC	-1.05 ± 0.05	19.6
NVSS J235702−372108	19.2 ± 0.2	18.3 ± 0.2	23:57:02.34	−37:21:11.8	9	PANIC	-1.10 ± 0.05	5.7
NVSS J235754−390134	18.8 ± 0.1	18.8 ± 0.3	23:57:54.51	−39:01:36.2	9	PANIC	-1.41 ± 0.04	< 2
NVSS J235945−330354	19.1 ± 0.2	18.4 ± 0.2	23:59:45.45	−33:03:56.8	15	IRIS2	-1.35 ± 0.05	2.5

[a] Two NVSS sources have been shown to be the components of a single radio source
[b] SuperCOSMOS optical position
[c] 2MASS position
[d] Obscured by an M star (see Paper III)
[e] 2MASS K magnitude in 8-arcsec aperture
[f] Fitted spectral index at 1400 MHz for sources with spectra that flatten at higher frequencies.
[g] Spectral indices from Klamer et al. (2006)
[h] These sources were observed by De Breuck et al. (2004, 2006) in the SUMSS-NVSS sample with no detection in K-band. We have reobserved them and improved the magnitude limit for NVSS J230527−360534.
[i] These sources were also part of the SUMSS-NVSS sample (De Breuck et al. 2004, 2006), and therefore were not reobserved in K-band. The K-band magnitudes and positions given are from De Breuck et al. (2004).
[j] α^{1400}_{843} where $\alpha_{5-\mathrm{point}}$ was not available from Paper I. For the sources from De Breuck et al. (2004), the spectral index has been recalculated using updated SUMSS flux measurements from the latest release.
[k] Position of the object discussed in Section 3.2, which may be a star.

poor weather conditions.
(3) The two-point observed-frame spectral index α^{8640}_{4800}.
(4) The seven-point observed-frame spectral index based on a linear fit to the 408, 843, 1384, 1400 and 2368 MHz flux densities from Paper I, as well as the 4800- and 8640-MHz data points. For those sources that have curved spectra that flatten (f) at high frequency, we use a quadratic fit to all seven data points to derive the observed-frame spectral index at 1400 MHz.
(5) The largest angular size (LAS). For single-component resolved sources, this is the deconvolved major axis of the elliptical Gaussian used to fit the source. For unresolved sources, we estimate a LAS upper limit of 1 arcsec. For multi-component sources, the LAS is the angular separation of the most widely-separated components. The LAS measured at 2368 MHz (see Paper I and Table 2) slightly underestimated the size of NVSS J1524354−352623 which has a LAS= 2.1 arcsec, while NVSS J111921−363139 is

found to be a 5.4-arcsec asymmetric double at higher resolution. Another case where we find an increase in the LAS for a compact source is NVSS J005509−361736; in Fig. A-2, this source is shown to be a very asymmetric double, with a LAS of 6.7 arcsec (as opposed to 2.8 arcsec in Paper I).
(6) The deconvolved position angle (PA) of the radio structure, measured from the north to the east. For multi-component sources, this is the orientation of the most widely-separated components used to calculate the LAS.

Note that in columns (5) and (6), we use the 8640 MHz images unless source components are resolved out at this frequency, in which case we use the 4800-MHz images.

Some of the sources which had uncertain identifications, and were observed with higher resolution at 4800 and 8640 MHz are shown in Fig. 3 and discussed further in Section 3.2. Overlay plots of the remaining 4800- and 8640-MHz observations are given in the Appendix (Fig. A-2).

3.2 Notes on individual sources

In Section 4.2 and Fig. 6 we look in detail at where the identification of a double-lobed radio source is statistically expected to be found. We have used that analysis in the following source notes.

NVSS J011415−373209: There are two objects which lie close to the axis joining the lobes, and closer to the fainter lobe than to the brighter. They have K-band magnitudes of 18.1 and 19.1. We have assumed the identification is the fainter object as it aligns with the axis of the lobes in the 8640-MHz image in Fig. 3. The fainter object is also closer to the NVSS centroid and the midpoint of the lobes than the brighter object and is therefore statistically more likely to be the identification (see Section 4.2).

NVSS J021759−301512: Several faint galaxies lie near the radio position. A uniform-weighted image separates the lobes, showing that the assumed identification is only 0.3 arcsec from the midpoint of the lobes, 1.3 arcsec south-east of the NVSS centroid and 0.2 arcsec from the radio axis.

NVSS J022825−302005: In the 2368-MHz image in Fig. 2, the distances of the identification from the midpoint (4.7 arcsec) and radio lobe axis (2.2 arcsec) are large compared to the distributions in Fig. 6. In Fig. 3, however, the 8640 MHz image shows the brighter object coincident with the radio core and confirms it as the identification.

NVSS J030037−310337: The radio structure is a wide separation triple source. There is a K-band counterpart coincident with the central radio component.

NVSS J031902−322319: The assumed K-band identification is very faint and diffuse, and is offset 2.7 arcsec from the centroid. While this offset is significant for a compact source, the uniform-weighted image is elongated slightly towards the identification. Assuming the identification is correct, we would expect the source to resolve into a double at higher resolution.

NVSS J103615−321659: The chosen identification is 3 arcsec from the NVSS centroid and the 2368-MHz image in Fig. 2 shows faint extension to the north-east. Therefore we expect this to be a double source with one very faint lobe. We also imaged this source at 4800 and 8640 MHz but found that any faint lobe was resolved out at these frequencies. Based on Fig. 6, a 3-arcsec offset is only 0.24σ from the mean of the distances from the NVSS centroid for the sample.

NVSS J103626−375819: The identification lies between the lobes and there is a fainter K-band object coincident with the stronger lobe. We assume that the object between the lobes is the counterpart since it is only 0.7 arcsec from the midpoint of the lobes and lies directly on the radio axis. The source would have been misidentified with this fainter object based on the 1384-MHz image alone, as the double structure was not apparent.

NVSS J104549−383853: There are two K-band objects between the lobes, on opposite sides of the radio axis. The brighter object is only 0.4 arcsec from the NVSS centroid, 1.4 arcsec from the midpoint of the lobes and 0.8 arcsec off the radio axis. Based on its better alignment with the high-resolution radio contours in Fig. 3 we select this brighter source as the identification.

NVSS J111921−363139: The overlay plot in Fig. 3 shows a broad extension of the K-band emission along the radio axis in both directions. This is discussed further in Section 4.3.

NVSS J130929−390222: In Figs. 2 and 3, the central component of this triple radio structure is coincident with a small cluster of four K-band features. The K magnitude was measured by centering on the four objects, all of which lie within the 4-arcsec-diameter aperture. The position listed in Table 2 is the fitted centroid of these four possibly associated objects.

NVSS J140223−363539: We believe the identification is the galaxy which is offset 2 arcsec south-west of the 2368-MHz peak in the direction that the 8640-MHz contours (see Fig. 3) are extended. A spectrum of this object will be presented in Paper III.

NVSS J140854−382731: Two K-band objects separated by 1 arcsec fall near the peak of the radio emission. The 4800-MHz image in Fig. 3 favours the brighter object as the identification.

NVSS J142312−382724: The assumed identification is a diffuse, possibly multiple, $K = 18.8$ galaxy directly along the axis between the lobes, closer to the fainter lobe and 4.3 arcsec from the midpoint. This is one of two radio galaxies that are outliers in Fig. 6(a), each with possible identifications that are $> 2.8\sigma$ from the mean of the distances from the NVSS centroid to the K identification. In this case, in addition to the claimed identification there is another very faint diffuse object along the axis between the lobes at $14^{\rm h}23^{\rm m}12.2^{\rm s}$ $-38^\circ27^{\rm m}26.8^{\rm s}$ (J2000), which is only 2.2 arcsec from the NVSS centroid, and 0.27 arcsec from the midpoint of the lobes. It is therefore closer to the midpoint position expected for the identification. The fainter object is too faint to measure ($K > 20$) and we have therefore tentatively listed the brighter object as the identification.

NVSS J142320−365027: The 8640-MHz image of this source in Fig. 3 reveals a core, confirming the identification. A jet extends towards the southern lobe and backflow is seen in the northern lobe, offset from the radio axis.

NVSS J144932−385657: The 4800-MHz image in Fig. 3 shows that the identification lies only 0.8 arcsec from the axis of the double source, and 0.4 arcsec from the NVSS centroid. Moreover, there are two faint K-band objects aligned with the north-east jet which are discussed further in Section 4.3.

Table 3. 4800- and 8640-MHz ATCA radio properties. The entries are explained in Section 3.1.

Source	S_{4800} (mJy)	S_{8640} (mJy)	α_{4800}^{8640}	α (7-point fit)	LAS (arcsec)	PA (°)
(1)	(2)		(3)	(4)	(5)	(6)
NVSS J001215−374113	10.5 ± 0.4	4.5 ± 0.4	-1.44 ± 0.16	-1.33 ± 0.02	1.1	52
NVSS J005402−361929	31.4 ± 1.1	14.0 ± 1.3	-1.37 ± 0.17	-1.23 ± 0.02	1.9	11
NVSS J005509−361736	50.3 ± 1.8	19.5 ± 1.8	-1.61 ± 0.17	···	6.7	−68
NVSS J011415−373209	28.0 ± 1.1	11.1 ± 1.3	-1.58 ± 0.21	-1.24 ± 0.02	27.3	−71
NVSS J022825−302005	24.2 ± 1.1	10.8 ± 1.4	-1.37 ± 0.23	-1.08 ± 0.03	23.8	−86
NVSS J101008−383629	33.3 ± 1.2	15.4 ± 1.5	-1.31 ± 0.18	-1.09 ± 0.02	11.6	−48
NVSS J103615−321659	10.6 ± 0.4	4.0 ± 0.4	-1.66 ± 0.18	-1.33 ± 0.02	10.4[a]	17
NVSS J104549−383853	36.9 ± 1.5	19.7 ± 2.2	-1.07 ± 0.20	-0.90 ± 0.02	20.1	−66
NVSS J105917−303658	15.3 ± 0.6	8.2 ± 0.8	-1.06 ± 0.18	-1.16 ± 0.02	1.0	27
NVSS J111921−363139	92.4 ± 3.2	33.2 ± 3.0	-1.74 ± 0.16	-1.42 ± 0.02	5.4	−26
NVSS J112641−383950	16.3 ± 0.6	6.6 ± 0.6	-1.54 ± 0.17	-1.34 ± 0.02	1.1	−42
NVSS J115829−374410	22.2 ± 0.8	9.3 ± 0.9	-1.48 ± 0.18	-1.32 ± 0.02	1.0	4
NVSS J130929−390222	43.9 ± 1.6	22.5 ± 2.0	-1.14 ± 0.16	-1.05 ± 0.02	21.6	33
NVSS J140223−363539	10.1 ± 0.5	4.3 ± 0.5	-1.45 ± 0.21	-1.32 ± 0.03	3.2	−48
NVSS J140854−382731	20.1 ± 1.0	6.4 ± 0.7	-1.95 ± 0.20	-1.30 ± 0.03	5.6	55
NVSS J142320−365027	61.7 ± 2.3	30.0 ± 3.4	-1.23 ± 0.20	-0.96 ± 0.02	25.6	22
NVSS J144206−345115	15.5 ± 0.6	9.6 ± 0.9	-0.82 ± 0.17	-0.93 ± 0.02	0.9	1
NVSS J144932−385657	21.5 ± 0.8	11.8 ± 1.1	-1.02 ± 0.17	···	6.8	48
NVSS J151020−352803	9.5 ± 0.4	6.0 ± 0.6	-0.78 ± 0.18	-1.27 ± 0.02	3.6	−75
NVSS J152435−352623	24.4 ± 0.9	15.0 ± 1.4	-0.82 ± 0.17	−1.12 (f)	2.1	0
NVSS J152445−373200	20.1 ± 0.8	11.2 ± 1.2	-0.99 ± 0.20	-1.01 ± 0.02	11.2	10
NVSS J204601−335656	15.3 ± 0.6	10.5 ± 2.1	-0.64 ± 0.35	-1.11 ± 0.03	1.6	−6
NVSS J210814−350823	32.1 ± 1.2	18.8 ± 3.8	-0.91 ± 0.35	-1.07 ± 0.02	5.9	15
NVSS J213238−335318	12.1 ± 0.5	7.5 ± 1.5	-0.81 ± 0.35	-1.42 ± 0.03	1.7	−75
NVSS J213637−340318	15.7 ± 0.6	8.9 ± 1.8	-0.97 ± 0.35	-1.28 ± 0.03	3.2	−41
NVSS J215249−343402	10.6 ± 0.4	6.5 ± 1.3	-0.83 ± 0.35	-1.41 ± 0.03	< 1	···
NVSS J232125−375829	43.8 ± 1.5	29.1 ± 2.6	-0.69 ± 0.16	−0.93 (f)	< 1	···
NVSS J233034−330009	16.6 ± 0.7	6.8 ± 0.6	-1.52 ± 0.16	-1.24 ± 0.03	15.3	−83
NVSS J234217−390810	23.5 ± 1.0	13.0 ± 1.6	-1.01 ± 0.22	-0.93 ± 0.03	33.0	−71

[a] LAS obtained from 2368 MHz image; see Table 2

NVSS J151020−352803: At 4800 MHz (Fig. 3) the radio morphology resolves into a double source. The K-band emission is extended along the radio axis (see Section 4.3).

NVSS J152445−373200: Two objects lie near the centre of the radio structure at 2368 MHz, one compact and one diffuse. The higher-resolution image in Fig. 3 was required to confirm that the correct identification is not the diffuse galaxy ~ 1.5 arcsec south-east of the core. Despite the stellar appearance of the identification, a colour image generated from deep $J-$ and K-band images reveals this object to be red like other galaxies in the field.

NVSS J213238−335318: The proposed identification is offset by 0.9 arcsec from the NVSS centroid but the radio source appears to be an incipient double at 8640 MHz (Fig. 3).

NVSS 213434−302522: The identification is 2 arcsec east of the peak in the 2368-MHz image. The elongated radio morphology suggests that the source would resolve into a double at higher resolution.

NVSS 215047−343616: The K-band image in Fig. 4 shows a faint extension $\sim$ 4-arcsec long, aligned with the radio jet axis, and directed towards the brighter NE lobe. This alignment is discussed further in Section 4.3.

NVSS J220412−363120: Blank field. A $K = 18.1 \pm 0.1$ galaxy lies at $22^{\rm h}04^{\rm m}12.01^{\rm s}$ $-36°31^{\rm m}16.0^{\rm s}$ (J2000),

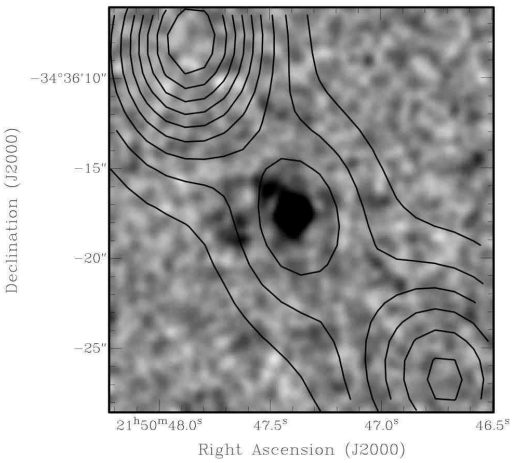

Figure 4. 2368-MHz ATCA contours of J215047−343616 overlaid on the PANIC K-band image as in Fig. 2 showing the central region where the K-band emission is extended along the jet axis.

6.5 arcsec west of the midpoint of the double-lobed radio structure and 7.4 arcsec from the NVSS centroid. These are 3.3σ and 2.7σ respectively from the mean values in Fig. 6. The K-band galaxy itself is > 4.4-arcsec in extent and it contributes to the 8-arcsec-aperture magnitude in Table 2. The accuracy of the astrometry on the IRIS2 and radio images is ± 0.3 arcsec and < 1 arcsec respectively. While we have treated the radio source as having no K-band identification, it is nevertheless possible that this very misaligned galaxy may be associated.

NVSS J221650−341008: The bright diffuse object marked in Fig. 2 is 1.0 arcsec from the midpoint of the lobes, and 0.6 arcsec from the radio axis and is therefore the assumed identification. The fainter object to the north is only 3 arcsec away and contaminates the 8-arcsec-aperture magnitude.

NVSS J233034−330009: On the basis of our original 13- and 20-cm images, we initially chose the identification to be the bright K-band object between the lobes and close to the brightest lobe. However, the higher-resolution image in Fig. 3 has revealed a weak core which is coincident with a faint peak in the K-band image with $K > 19$.

NVSS J234217−390810: The high-resolution 4800-MHz image in Fig. 3 was required to identify a core coincident with a $K = 17.4 \pm 0.1$ galaxy. Both lobes show backflow towards the core.

3.2.1 Interlopers in the sample

While our selection method is necessary to extract the best high-redshift candidates from large radio catalogues, there will unfortunately always be interlopers that contaminate the sample. In Paper I we already identified several sources which were excluded from our sample. Here we discuss another three sources that have been excluded.

Each of the sources below and in Fig 5 are in the NVSS catalogue and were listed in our MRCR–SUMSS sample in Paper I. However, they have each turned out to be individual lobes of a giant double or triple source. Our selection process is designed to eliminate catalogue sources which are actually a single lobe of a large double or triple, by removing sources which have another source within 100 arcsec. Then every source was examined with the NVSS contours overlaid on a 6-arcmin field from SuperCOSMOS. At this stage there were several sources eliminated as they clearly had a second lobe within 3 arcmin. Several other sources had an elongated morphology characteristic of a lobe, and a second lobe was then identified in a larger image. These steps are, in general sufficient to remove most sources which are lobes of a double.

NVSS J205410−393530: This is the lobe of an 8.60-arcmin source which has a core, lobes and hotspots along the jets. There is a K-band object at $20^{\rm h}54^{\rm m}10.67^{\rm s}$ $-39^\circ35^{\rm m}34.0^{\rm s}$ (J2000) that appeared to align with the radio source, and the magnitude of this object was measured with PANIC to be 19.5 ± 0.4. Once we discovered NVSS J205410−393530 is in fact a lobe, the core of the giant source was found to have an identification at $20^{\rm h}53^{\rm m}59.07^{\rm s}$ $-39^\circ30^{\rm m}18.1^{\rm s}$ (J2000) with a 2MASS K-band magnitude of 13.58 ± 0.05. A spectrum has identified this object to be a $z = 0.167$ QSO, with a linear size of 1.46 Mpc and a 1.4-GHz luminosity of 1.2×10^{25} W Hz^{-1}. The new total flux densities at 843 and 1400 MHz are 232 ± 7 and 160 ± 4 mJy respectively, including all the source components, giving $\alpha_{843}^{1400} = -0.73 \pm 0.08$.

NVSS J212553−311043: The source listed in Paper I has turned out to be the southern lobe of a triple with a largest angular size of 3.9 arcmin. The identification is at $21^{\rm h}25^{\rm m}53.72^{\rm s}$ $-31^\circ08^{\rm m}58.9^{\rm s}$ (J2000) and has magnitudes of $K = 14.6 \pm 0.1$ (2MASS), $B_J = 18.7$ and $R = 17.9$ (SuperCOSMOS). The total flux densities at 843 and 1400 MHz are 106 ± 6 and 91 ± 3 mJy respectively, resulting in a flat spectral index of -0.30 ± 0.13.

NVSS J233238−323537: This source was missed as a lobe of a double because, firstly, the lobes are separated by 4.15 arcmin and, secondly, because the source from the NVSS catalogue appears to be compact and round with no extension. Once it was imaged in K-band with no identification, and the ATCA images displayed low-surface-brightness characteristic of backflow emission, it was clear that we were seeing one lobe of a wide-separation double. The total NVSS and SUMSS flux densities are 114 ± 3 and 160 ± 4 mJy respectively, giving $\alpha_{843}^{1400} = -0.67 \pm 0.07$. There is a bright object along the radio lobe axis at $23^{\rm h}32^{\rm m}30.57^{\rm s}$ $-32^\circ33^{\rm m}35.77^{\rm s}$ (J2000), which is an M star, and the radio galaxy host has not been identified.

3.2.2 A misidentification

In Paper I we suggested that the double-lobed source, NVSS J101215−394939 had an identification in SuperCOSMOS. While the listed identification is along the radio lobe axis, that object has since been shown to have a stellar spectrum and, therefore, is not the correct counterpart. This source will require K-band imaging to find the correct identification.

4 DISCUSSION

4.1 Spectral energy distributions

In Paper I, we fitted the spectral energy distributions (SEDs) from 408 to 2368 MHz. We have now redone these fits with the addition of the new 4800- and 8640-MHz data. Of the 29 sources in Table 3, 25 (86 per cent) can be fitted with a single power law between 408 and 8640 MHz in the observed frame. Two sources are found to flatten at higher frequencies, which may indicate an increased contribution from a core and/or hotspots. The remaining two sources (NVSS J005509−361736 and NVSS J144932−385657) can not be fitted with a linear or a quadratic function, as was the case in Paper I between 408 and 2368 MHz.

Our results are consistent with Klamer et al. (2006) who found 89 per cent of the 37 SUMSS–NVSS sources were well characterized by a single power law, while the remainder flattened at higher frequencies. This is despite the fact that Klamer et al. (2006) used matched-resolution ATCA observations between 2368 and 18 496 MHz, while our ATCA observations both in Paper I and this paper were all made with a 6 km array configuration. Thus, while some source components are clearly resolved out at high frequency (see Figs. 3 and A-2), the effect is not significant enough to alter the shapes of the SEDs.

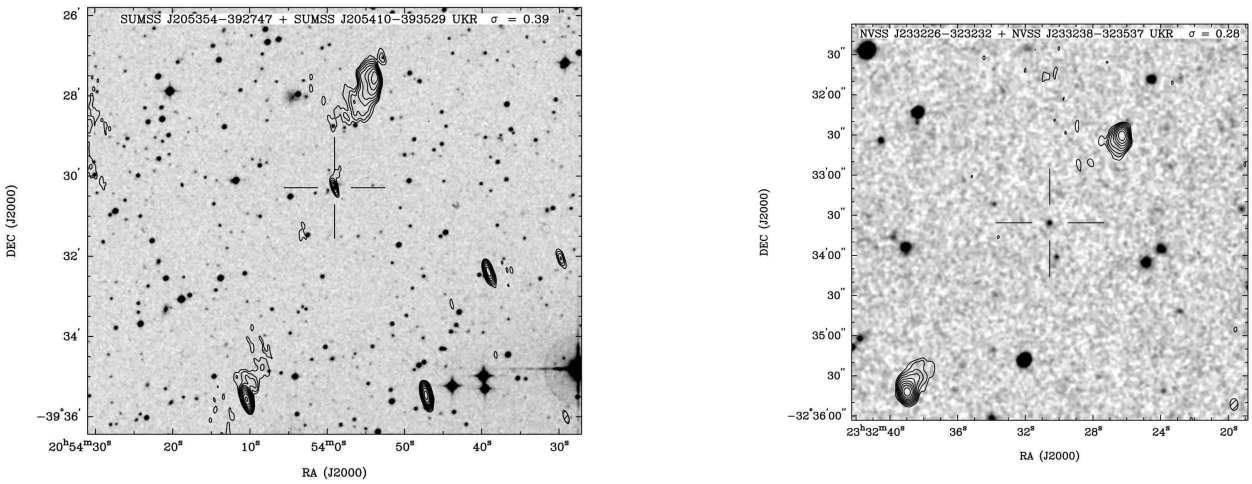

Figure 5. Smoothed SuperCOSMOS UKR images are overlaid with the 1384-MHz (left image) and 2368-MHz (right image) ATCA contours for two of the sources found to be interlopers in the sample. The lowest contour is 3 sigma, and the contours are a geometric progression in $\sqrt{2}$. The rms noise (σ) is shown in the header of each image in mJy beam^{-1}. The ATCA synthesized beam is shown in the bottom right-hand corner of each panel. Left: NVSS J205410−393530 was similarly found to be one component of the south-east lobe of this giant source which has a core, lobes and multiple hotspots. The identification is a $z = 0.167$ QSO, marked by the cross-hairs. Right: The source NVSS J233238−323537 in Paper I had been found to be the south-east lobe of this giant double source. The north-west lobe is listed in NVSS as a separate source, NVSS J233226−323232. The south east lobe is compact and round in the NVSS image, but the ATCA image reveals low-surface-brightness emission extended towards the other lobe. The marked object is a star and the host galaxy has not been identified.

4.2 Identification of the host galaxies

The environments around HzRGs are likely to be denser and more disturbed than around nearby radio galaxies (e.g. Carilli et al. 1997; Pentericci et al. 2001; Röttgering et al. 2003). Therefore the expected position of the optical counterparts relative to the radio emission may not obey the same rules as found in low-redshift samples such as 3C (Laing, Riley & Longair 1983) and the Molonglo Southern 4Jy sample (MS4; Burgess & Hunstead 2006). In previous HzRG studies, the process of identifying the hosts of USS radio galaxies from K-band images has been typically based only on which K object aligns best, by eye, with the radio contours. In order to quantify this process statistically, we have measured the location of the identified host galaxy relative to the features of the radio emission for the double sources in our sample. This information has then been used to assess the reliability of identifications for which there are several nearby K-band candidates or where the potential identification is offset from its expected location; for example, one may tend to look for an identification closer to the brighter radio lobe. Our aim was to assess how far a potential identification could be displaced from the radio features, and still be considered statistically likely to be the identification.

The most difficult decisions arise in complex double structures rather than compact sources in which the centroid is well defined. In order to get a statistical picture of the locations of potential identifications, angular separations were measured from the identification to several features of the radio structure for all of the double sources in our sample. The first of these features is the radio centroid; since our sample consists mostly of sources $\leqslant 1$ arcmin in size, NVSS is expected to record an accurate 1.4-GHz centroid position. Next we found the angular distances from the identification to the midpoint of the lobes, and the 'midway point' defined by Burgess & Hunstead (2006) to be halfway between the midpoint and the centroid. Lastly, the perpendicular distance of the identification from the axis joining the lobes was measured. The resulting distributions of these distances are shown in Fig. 6, with the accompanying statistics in Table 4.

In Table 4, the median, mean and standard deviations are given for the distributions of distances to identifications in our sample. The midpoint has the lowest median and mean, indicating that it is statistically a more likely place to find the identification compared to the midway point or centroid. Burgess & Hunstead (2006) found the most likely position for the optical identification for the MS4 was the 'midway point', based on a smaller median and mean distance. The difference between both the means and standard deviations for the 'midway point' and the midpoint in our sample is negligible. It is interesting that the centroid position is the least likely of the three locations to find the optical counterpart, suggesting that low-surface-brightness emission is less important in finding the correct identification. 66 per cent of optical counterparts lie within 2 arcsec of the midpoint of the lobes, while only 48 per cent are as close as this to the centroid.

The statistics for the normalised angular distances to the brighter and fainter lobes are indistinguishable. Therefore, it cannot be assumed that the identification would lie closer to the brighter lobe. Furthermore, Fig. 6(e) confirms that while the optical counterpart is most likely to lie close to the midpoint of the lobes, the tail of the distribution is not biased towards either lobe. We used this information extensively in Section 3.2 in order to resolve uncertain identifications.

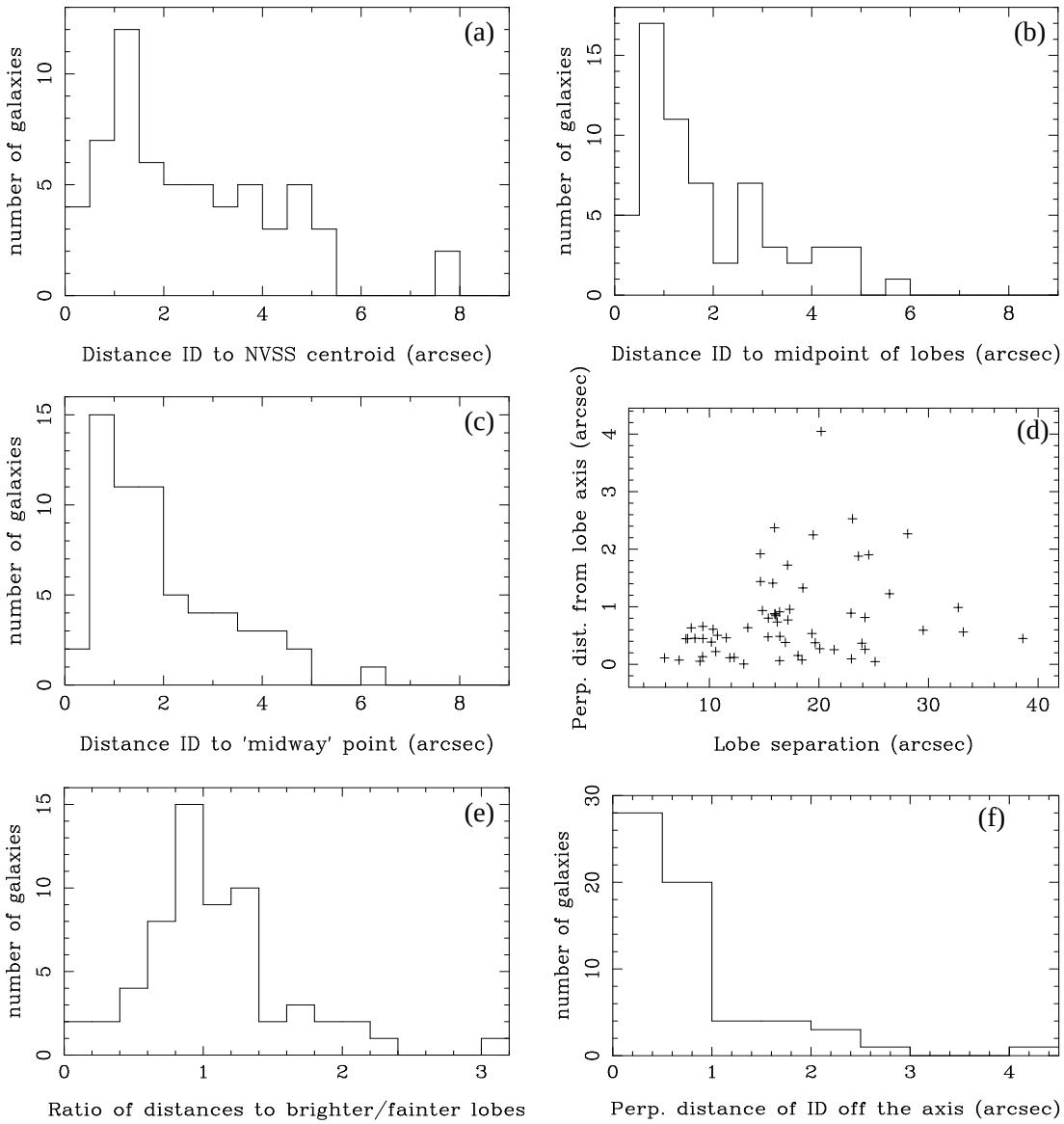

Figure 6. Histograms of the angular distances from the proposed K-band identification to (a) the NVSS centroid, (b) the midpoint of the lobes, and (c) the 'midway point' (half way between the centroid and the midpoint). (d) Distance between the lobes versus the perpendicular distance of the identification from the axis joining the lobes, for the double sources in our sample. (e) Histogram of the ratio of the distance to the brighter lobe to the distance to the fainter lobe. (f) Histogram of the perpendicular distance of the identification from the axis of the lobes.

There are two clear outliers in the NVSS centroid histogram (Fig. 6(a)) with distances to the centroid more than 2.7σ from the mean. The first, NVSS J142312−382724 was discussed in Section 3.2. The second is NVSS J024811−335106 which is a 33.2-arcsec double. The lobes are uneven in strength and both show backflow (see Fig. 2); the NVSS centroid lies on the radio axis but much closer to the brighter lobe than the midpoint. The identification is only 2.0 arcsec from the midpoint of the lobes and is 0.6 arcsec from the radio lobe axis. We are very confident of the identification.

In Fig. 6(f), 79 per cent of the double sources have identifications within 1 arcsec of the axis joining the lobes. All of the sources in Fig. 6(d) that are more than 0.7 arcsec from the radio axis have lobe separations > 14 arcsec, and the median distance from the radio axis for lobe separations of > 14 arcsec is 0.81 arcsec compared to 0.45 arcsec for those with lobe separations < 14 arcsec. This indicates that the larger sources are more likely to have complex morphologies which can affect the measurements of lobe positions.

4.3 Alignment effect

The nature of the link between the presence of a supermassive black hole and the evolution of its massive elliptical galaxy host remains uncertain. However, a relationship among the AGN, radio jets and the host galaxy has been inferred from the 'alignment effect' in which the position angle of the major axis of an elliptical host galaxy has been found to align with the radio jet axis (McCarthy et al.

Table 4. Mean, median and standard deviation for the distributions of distances from the K-band identification to the three radio positions – NVSS centroid, lobe midpoint and 'midway point' – in Fig. 6, given in arcsec. The values for the distances to the brighter and fainter lobes have been normalised to the lobe separation.

Radio position	Mean ($''$)	Median ($''$)	σ
NVSS centroid	2.6	2.4	1.8
Midpoint	1.9	1.4	1.4
'Midway point'	1.9	1.6	1.3
Radio position	Normalised		σ
	Mean	Median	
Brighter lobe	0.49	0.50	0.12
Fainter lobe	0.51	0.51	0.13

1987; Chambers, Miley & van Breugel 1987). Alignments are also seen in near-infrared USS-selected HzRG samples (De Breuck et al. 2002), and in high resolution HST images of HzRGs in the optical (e.g. Best, Longair & Röttgering 1996) and near-infrared (e.g. Pentericci et al. 2001; Zirm, Dickinson & Dey 2003). In contrast Eales et al. (1997) found no significant alignments in the B2/6C sample, but their sample was small and their near-infrared images were not as deep as those above.

At low redshift, near-infrared wavebands sample the evolved stellar population which is unlikely to be affected by the radio jets. At high redshift ($z > 2.5$), however, the observed near-infrared is dominated by young stars that may result from the radio jet impacting the dense interstellar and intergalactic medium surrounding the active nucleus. In the early universe, gas densities in forming galaxies and protoclusters were much higher than in the nearby universe and shocks associated with the radio jets are more likely to have triggered star formation along their path (Bicknell et al. 2000; Klamer et al. 2004; Croft et al. 2006). van Breugel et al. (1998) found a strong evolution with redshift in the near-infrared alignments of radio host galaxies, with smoother, less elongated host galaxy morphologies occurring at $z < 3$. In contrast, Pentericci et al. (2001) found no difference between radio-infrared alignments in $z < 3$ and $z > 3$ galaxies. The absence of alignments in the Eales et al. (1997) B2/6C sample, and their clear presence in the 3C sample (Dunlop & Peacock 1993), led Eales et al. (1997) to argue that alignments occur only in the most luminous radio sources. While De Breuck et al. (2002) disagree with that interpretation, we will consider in Paper III the luminosity dependence of alignments for those sources with measured redshifts.

We now present an analysis of radio-infrared alignments for the MRCR–SUMSS sample. While such an analysis would ideally be done at the highest possible spatial resolution, the number of HzRGs that can be studied with HST is small. The statistical advantage of investigating alignments in the MRCR–SUMSS sample is the large sample size. Position angles of the host galaxy were measured on the smoothed K-band images by fitting ellipsoidal profiles using the IRAF/STSDAS task ELLIPSE and taking the major axis as the position angle of the host. The position angle, ellipticity and centre of the ellipse were allowed to vary, and ellipses were fitted as a function of radius. We typically found that a central ellipse could be fitted with a defined position angle, but as the radius increased there were one or two sudden steps in the position angle. In these cases, we took the outermost radius at which an ellipse could be fitted with a stable ellipticity and position angle. For some images the position angle was constantly changing with radius and no stable ellipse could be fitted. The galaxies that could not be fitted included those with low K-band signal-to-noise ratio, and those with clumpy, circular or disturbed morphologies.

Of the 152 sources with PANIC or IRIS2 K-band imaging, we fitted position angles to 131 K-band images, of which nine did not have a well defined radio axis. For the remaining 122 sources we measured the offset between K-band and radio position angles. Fig. 7 shows the distribution of differences between the position angle of the radio axis and the major axis of the fitted K-band ellipsoid. While some samples in the literature show alignments over angles from 0–30 degrees (e.g. De Breuck et al. 2002) we find a more uniform distribution of offset angles, with a small excess of alignments within 10 degrees. This excess suggests that the process causing the alignment of the outermost isophotes of the host galaxy is tightly collimated along the radio jet axis, as might be expected for jet-induced star formation. Alternatively, the small alignment angles could be the result of radio jets having broken through gas clouds along their path, leaving an increased surface area of cooled gas for scattering light from the active nucleus (Bremer, Fabian & Crawford 1997).

The sources in our sample with LAS > 5 arcsec have the same percentage (21 per cent) aligned within ten degrees as in the complete sample. This is in contrast to other papers (e.g. De Breuck et al. 2002) where the larger sources have been found to be more strongly aligned. To test whether the ellipsoidal fitting may have missed faint emission with low signal-to-noise, we rotated all the smoothed K-band images to align with the radio position angles. The images were then co-added after careful scaling by the background level and the galaxy peak brightness. The result showed no ellipticity, confirming that alignments are not present in the bulk of our sample. As most of the sources in our sample are at $z < 3$, this result is consistent with the ground-based sample of van Breugel et al. (1998) but in stark contrast to Pentericci et al. (2001) who found a predominance of aligned features in their near-infrared HST images. We attribute this difference to the different surface brightness sensitivities and resolutions of HST and ground-based images.

Nine galaxies in our sample (listed in Table 5) show K-band emission extending beyond the host galaxy ellipsoid. In these cases the overall position angle was estimated by eye, and the distribution of offsets from the radio axis is shown in Fig. 7. Four of the nine have position angles within 10 degrees of the radio position angle, and seven are within 30 degrees. The origin of these alignments could again be the result of jet-induced star formation or scattered nuclear light along the path of the radio jets. The misaligned cases may be due to changes in jet direction, or the chance projection of other objects close to the line of sight to the host galaxy.

NVSS J111921−363139 (see Fig. 3) has extended K-band emission which can not be fitted by an ellipsoid, with broad patches of emission lined up along the radio axis. This

Table 5. Position angle offsets between the radio axis and, firstly, the extended K-band emission ($\delta\mathrm{PA_{ext}}$) and, secondly, the major axis of the host ellipsoid ($\delta\mathrm{PA_{ellipse}}$) for the galaxies that have extended K-band structure extending beyond the host galaxy ellipsoid.

Object	$\delta\mathrm{PA_{ext}}$ (degrees)	$\delta\mathrm{PA_{ellipse}}$ (degrees)
NVSS J004000−303333	19	42
NVSS J004030−304753	22	34
NVSS J021208−343111	34	0.8
NVSS J140010−374240	62	59
NVSS J144932−385657	8	31
NVSS J151020−352803	5	15
NVSS J215047−343616	9	0.5
NVSS J221650−341008	23	30
NVSS J234235−384526	5	15

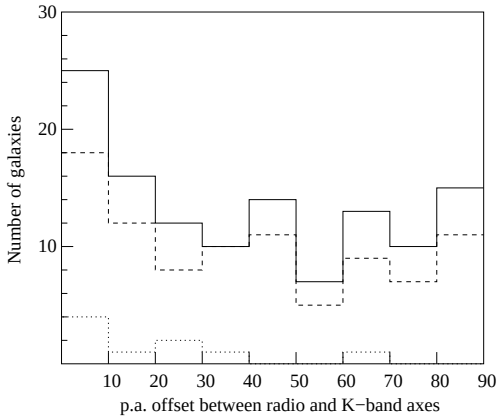

Figure 7. Distribution of differences between the radio axis position angle and the major axis of the K-band fitted ellipsoid for 122 galaxies from the MRCR–SUMSS sample (solid line) and for those with largest angular size greater than five arcsec (dashed line). The dotted line shows the difference between the radio position angle and that of the extended K-band emission for the nine sources which have this feature.

morphology has been previously associated with either ionisation cones or the presence of dust in the host galaxy. At the redshift of the host galaxy ($z = 2.769$) there are no prominent emission lines in the Ks-band filter, so we may be seeing either an inclined dust lane, through which the nucleus can be seen (similar to ESO 248-G10, Bryant & Hunstead 2000), or widely distributed dust and star formation along the radio jet axis.

4.4 Aperture corrections

In some earlier papers (e.g. Eales et al. 1997; Willott et al. 2003; De Breuck et al. 2004) the K-band magnitudes have been converted to an equivalent 64-kpc aperture value. This value was chosen by Eales et al. (1997) because it corresponds to an 8-arcsec aperture at $z = 1$. Fig. 8, based on data from De Breuck et al. (2006), shows that the actual correction to the K-band magnitudes is quite small and applies over the full magnitude and redshift range. The basis of the empirical correction adopted by Eales et al. (1997) is that the integrated emission of galaxies at $z > 0.6$ within an aperture of radius r is proportional to $r^{0.35}$. While a profile of this form may be an acceptable fit to nearby, bright galaxies, the galaxies in our sample are faint and distant, and the $K-$band images are not deep enough to justify fitting such a profile.

At high redshift ($z > 2$) it is expected that many galaxies are still in the process of merging and have not yet relaxed to an elliptical profile (e.g. van Breugel et al. 1998; Pentericci et al. 1998). An $r^{0.35}$ profile is therefore unlikely to apply over an epoch range as large as $z = 0.6$–4. This is supported by van Breugel et al. (1998) who found that the surface brightness profiles of $z < 3$ HzRGs are steeper than those at $z > 3$. The assumption of a 'universal' radial profile then introduces an added error, estimated to be as large as 20 per cent. A contribution to this error comes from the chosen starting aperture which could, in principle, be based on the profile of the galaxy. The practical issue, however, is that profiles can not be determined accurately for the faint and distant galaxies. As a result, some authors have adopted an 8-arcsec aperture from which to convert to a 64-kpc aperture based on the simplicity of their equivalence at $z = 1$. In practice an 8-arcsec aperture is often too large to avoid including additional flux from nearby galaxies. De Breuck et al. (2002, fig. 1) showed that the majority of HzRGs in their sample have most of their flux contained within a 2-arcsec aperture.

In Fig. 9 we plot the radial profiles of our K-band identifications with $K > 19$ and $K < 17$ representing nominal high- and low-redshift groups respectively. Almost all the galaxies have their total emission enclosed by a 4-arcsec aperture, with no difference between the brighter and fainter sources. Infrared imaging is relatively insensitive to low-surface-brightness emission, and for most of our objects, the flux has dropped to the background sky level within a 4-arcsec aperture. On the other hand, there are frequent cases where the intensity increases again beyond a radius of 2 arcsec, indicating contaminating emission from a nearby source. For the sources in our sample, therefore, we do not believe there is any significant missing flux in the 4-arcsec apertures. Extending the aperture to 8-arcsec adds sky noise, which increases the error.

Over the large time interval from $z \sim 4$ to the present, galaxies undergo significant evolution. We have no evidence that one physical size scale is a reasonable representation of HzRGs which may range over a factor of ten in mass

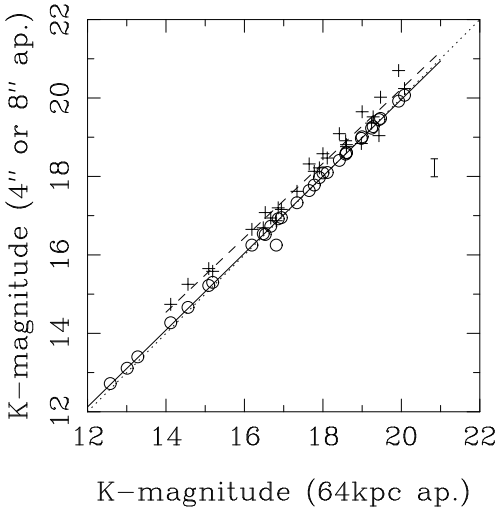

Figure 8. K-band magnitudes corrected to 64-kpc apertures versus 8-arcsec (circles) and 4-arcsec (+) apertures from the SUMSS–NVSS data set (De Breuck et al. 2004, 2006). The solid line is the linear fit to the 8-arcsec points, the dashed line is the fit to the 4-arcsec-aperture points, while the dotted line is the line of equality. An error bar represents the average error in the 8-arcsec-aperture K-band magnitudes. It is clear that the difference between the 8-arcsec- and 64-kpc-aperture $K-$magnitudes is small compared to errors. The 4-arcsec-aperture values follow a very similar gradient, with a fit equation $K(64\,\mathrm{kpc}) = 1.026 * \log[K(4'')] - 0.824$.

(Rocca-Volmerange et al. 2004) and which we observe at different evolutionary stages in their formation. For these reasons, we have chosen not to use 64-kpc-aperture magnitudes, and instead to use 4-arcsec-aperture magnitudes in this paper.

4.5 K and flux density distributions

Essentially all USS-selected HzRG samples have selection biases resulting from the different spectral index cut-offs and selection frequencies, which results in samples with vastly different flux density distributions. A k-correction was thought to underpin the effectiveness of USS-selection as a steepening radio SED would be shifted with redshift to lower frequencies and therefore the highest redshift objects would be steepest at a given observed frequency (Gopal-Krishna 1988; Carilli et al. 1999). Therefore USS samples selected at lower frequencies should net a higher redshift distribution. This theory was challenged by Klamer et al. (2006) who found that the SEDs of sources in the 843-MHz-selected SUMSS–NVSS sample are predominantly straight. The MRCR–SUMSS sample was then selected at the lower frequency of 408 MHz, and the resulting K-band magnitude and 1400 MHz flux density distributions are compared in Fig. 10. The other samples shown are USS-selected samples with 4-arcsec-aperture magnitudes including the SUMSS–NVSS, 6C** (Cruz et al. 2006) and De Breuck et al. (2001, 2002) samples, along with the three non-USS-selected samples from McCarthy et al. (1996; 2007, private communication), CENSORS (Brookes et al. 2006, 2008) and a combined sample from the 3CRR, 6C*, 6CE and 7CRS catalogues (compiled by Willott et al. 2003). The McCarthy sample is a set of 277 K-band observations of radio galaxies, of which 175 have redshifts. While it remains unpublished, it is the largest non-USS K-band sample and therefore provides an interesting comparison with the other samples discussed here. We obtained 1400 MHz flux density values for the McCarthy sample by cross-matching the positions with the NVSS catalogue within a 60-arcsec search radius. For the 38 of the 293 sources which had two matches within 60 arcsec, we selected the closest match. SUMSS–NVSS was selected to have $\alpha_{843}^{1400} < -1.3$, and the 6C** sample is from the 151-MHz 6C survey with $\alpha_{151}^{1400} < -1.0$. The De Breuck et al. (2001, 2002) sample was selected at one of the frequencies 325, 365, or 408 MHz as detailed in the papers, and has $\alpha_{\sim 350}^{1400} \lesssim -1.3$. The combined sample compiled by Willott et al. (2003) includes 202 narrow line galaxies from the 3CRR, 6C*, 6CE and 7CRS catalogues, selected at 151 and 178 MHz. The 1400 MHz flux densities were obtained from the NASA/IPAC Extragalactic Database (NED) by selecting the most recently published[3] total integrated flux density. In several cases only peak flux densities were available and 26 targets have no published observations at 1400 MHz. While the 3CRR/6C*/6CE/7CRS combined sample is less complete in 1400 MHz flux density than the other samples shown in Fig. 10, it has a more complete redshift follow-up (see Paper III).

The four USS samples have very similar K-magnitude distributions, which may suggest that when the redshift followup is complete, the redshift distributions may also be similar. A Kolmogorov-Smirnov test comparing the K distributions of the other samples with the MRCR–SUMSS sample, suggests that the three other USS-selected samples (SUMSS–NVSS, 6C** and De Breuck 2001, 2002) are likely to be drawn from the same distribution as the MRCR–SUMSS data, with p values of 0.57, 0.75 and 0.59. However, the three non-USS-selected samples (CENSORS, 3CRR/6C*/6CE/7CRS and McCarthy) are not from the same distribution, with $p < 0.0005$. The MRCR–SUMSS sample is much larger than the other USS-selected samples in terms of the number of K measurements, and therefore will give a more complete picture of USS radio galaxy redshift distributions once the spectroscopic followup is complete.

The most striking result is that even though the USS-selected samples each have completely different selection criteria and vary by a factor of 3.5 in median flux density, the resultant K-band distributions are the same, and are fainter than for the non-USS-selected samples. The non-USS-selected samples have vastly different flux density distributions, but have similar K-band medians that are brighter than the USS-selected samples. Therefore the effectiveness of USS-selection in identifying fainter and potentially higher-redshift galaxies in the samples shown, is not dependent on the selection frequency or the resultant flux density distributions of these samples. Based on the $K - z$ relation, if this result also applies to the redshift distribution, then it will provide strong evidence against the

[3] Flux densities came from Condon et al. (1998), Laing & Peacock (1980), Kellermann, Pauliny-Toth & Williams (1969), White & Becker (1992), Owen & Ledlow (1997), Croston et al. (2005) and Becker, White & Helfand (1995)

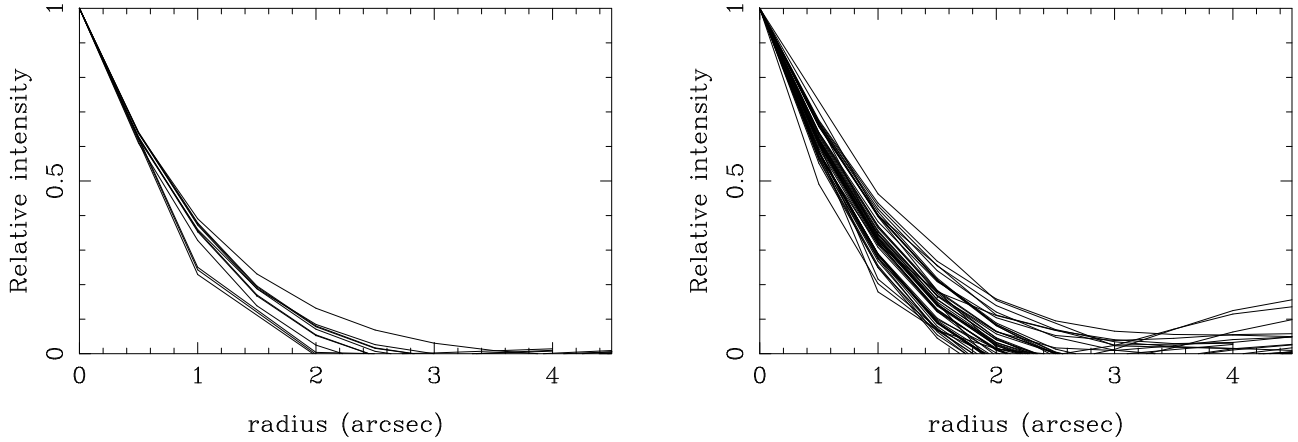

Figure 9. Relative intensity at each radial step is plotted against radial steps of 0.5 arcsec for all of the PANIC and IRIS2 images with $K < 17$ (left) and $K > 19$ (right). In almost every case the emission from the galaxy is contained within a 4-arcsec-diameter aperture, and in some cases, emission from nearby objects is beginning to contaminate an 8-arcsec-diameter aperture.

k-correction theory which has been thought to account for the effectiveness of USS-selection.

5 CONCLUSIONS

K-band imaging has been presented for a large Southern hemisphere USS-selected HzRG survey, the MRCR–SUMSS sample (408–843 MHz). We have the following findings:

(1) Based on 163 new K images, 152 radio sources (93 per cent) have K-band identifications with the faintest at $K = 21.4$. In combination with the 12 previously-published observations, 175 targets have followup observations and 94 per cent of these have detections. This is consistent with the 96 per cent detection rate of all $z > 2$ HzRGs to $K = 22$ in the literature (Miley & De Breuck 2008).

(2) We have investigated the location of the identifications in relation to the radio structures for double sources and found that the midpoint of the lobes is the most likely place to find the identification, with 66 per cent of counterparts located within 2 arcsec of the midpoint. The radio centroid is a less likely position to find the identification. We have used this analysis as a guide when selecting identifications in cases where there were ambiguities.

(3) We find that the identification is no more likely to be closer to the brighter lobe than the fainter one, even though selection of the identification by eye may favour an identification closer to the brighter lobe. While 79 per cent of identifications are within 1 arcsec of the axis joining the lobes, the off-axis distance increases for sources with larger lobe separations.

(4) The size of the MRCR-SUMSS sample is larger than most previous samples that have investigated the alignment effect between radio and near-infrared axes. We have found that 21 per cent of the galaxies that could be fitted with an ellipsoid, have a major axis that aligns within 10 degrees of the radio axis. There is no evidence for alignment at angles larger than 10 degrees, lending support to jet-induced-star-formation as the origin of the alignment. We identify non-elliptical, extended aligned structures in nine galaxies that cannot all be explained by jet-induced-star-formation.

(5) By comparing the MRCR–SUMSS sample K-band and 1400 MHz flux density distributions with those of other USS-selected and non-USS-selected samples, we find that while the flux density distributions vary significantly between samples due to different selection criteria, the median K-band magnitudes are similar for all the USS-selected samples. If the success of USS-selection is due to a k-correction, we would expect the samples selected at lower frequency to have a fainter magnitude distribution. This needs to be tested further with comparative redshift distributions.

Paper III will present spectroscopy for this sample and interpret the radio and K-band results in terms of the redshifts found.

Acknowledgements

We acknowledge financial support from the *Access to Major Research Facilities Programme* which is a component of the *International Science Linkages Programme* established under the Australian Government's innovation statement, *Backing Australia's Ability*.

Australian access to the Magellan Telescopes was supported through the Major National Research Facilities program of the Australian Federal Government.

JWB acknowledges the receipt of both an Australian Postgraduate Award and a Denison Merit Award. RWH, HMJ and JJB acknowledge support from the Australian Research Council and the University of Sydney Bridging Support Grants Scheme. BMG acknowledges the support of a Federation Fellowship from the Australian Research Council through grant FF0561298.

We thank Elaine Sadler for many useful discussions, Pat McCarthy for providing his unpublished data sample, David Crawford for providing the MRCR, Gemma Anderson for doing some observations for us, and the team at the Magellan Telescopes for their exceptional efficiency and good humour. We also thank the referees for their valuable comments which improved the paper.

The Australia Telescope Compact Array is part of the Australia Telescope which is funded by the Commonwealth of Australia for operation as a National Facility managed by CSIRO. SuperCOSMOS Sky Survey material is based on photographic data originating from the UK, Palomar and

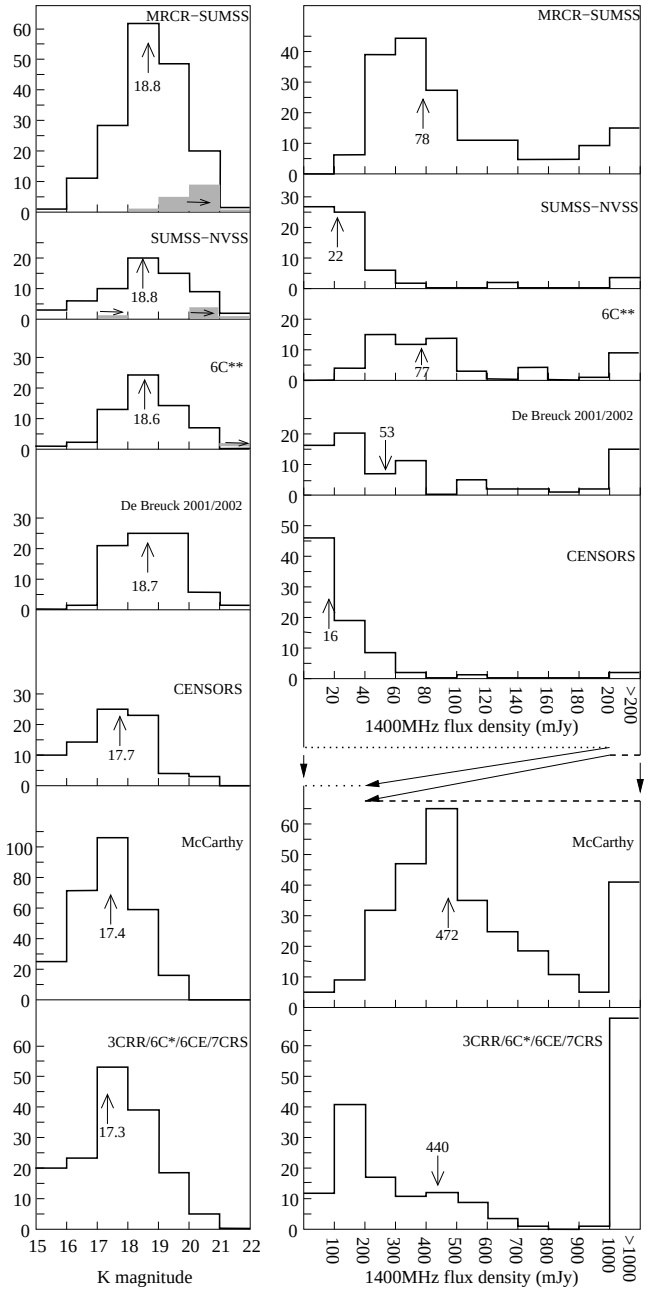

Figure 10. Distributions of NVSS-1400-MHz-flux densities and K-band magnitudes for the samples from MRCR–SUMSS, SUMSS–NVSS (De Breuck et al. 2004, 2006), De Breuck et al. (2001, 2002), 6C** (Cruz et al. 2006), CENSORS (Brookes et al. 2006, 2008), McCarthy et al. (1996; 2007, private communication) and a combined sample from the 3CRR, 6C*, 6CE and 7CRS catalogues (compiled by Willott et al. 2003). The 4-arcsec-aperture values for the MRCR–SUMSS, SUMSS–NVSS and De Breuck et al. (2001, 2002) samples are shown, while the plots for the 6C** and CENSORS samples show 4-arcsec-aperture magnitudes calculated from the published 3- and 5-arcsec values by averaging the equivalent 3- and 5-arcsec fluxes and converting to a 4-arcsec magnitude. The McCarthy magnitudes are in a 3-arcsec aperture and based on our dataset, we expect the average offset between the 3-arcsec and 4-arcsec aperture magnitudes to be < 0.2. The combined 3CRR/6C*/6CE/7CRS sample from Willott et al. (2003) has equivalent 64-kpc aperture K-band magnitudes, which are expected to be an average of 0.4 magnitudes fainter than the equivalent 4-arcsec-aperture magnitudes for those objects (see Fig. 8). Vertical arrows mark the median values in each plot, calculated from the confirmed values and excluding lower limit K magnitudes shown by the shaded regions. The non-USS samples contain sources brighter than $K = 15$, and they are included in the median calculation. The CENSORS sample has one source with 5 K-band components and hence there are 4 fewer sources in the flux density histogram than in the K-band histogram. The 3CRR/6C*/6CE/7CRS sample has 26 sources that do not have published 1400-MHz flux densities and are included in the K-band histogram, but not the flux density histogram.

ESO Schmidt telescopes and is provided by the Wide-Field Astronomy Unit, Institute for Astronomy, University of Edinburgh. This research has made use of the NASA/IPAC Extragalactic Database (NED) which is operated by the Jet Propulsion Laboratory, California Institute of Technology, under contract with the National Aeronautics and Space Administration. IRAF is distributed by the National Optical Astronomy Observatories, which are operated by the Association of Universities for Research in Astronomy, Inc., under cooperative agreement with the National Science Foundation. This publication makes use of data products from the Two Micron All Sky Survey, which is a joint project of the University of Massachusetts and the Infrared Processing and Analysis Center/California Institute of Technology, funded by the National Aeronautics and Space Administration and the National Science Foundation.

REFERENCES

Becker R. H., White R. L., Helfand D. J., 1995, ApJ, 450, 559
Best P.N., Longair M.S., Röttgering H.J.A., 1996, MNRAS, 280, L9
Bicknell G. V., Sutherland R. S., van Breugel W. J. M., Dopita M. A., Dey A., Miley G. K., 2000, ApJ, 540, 678
Blumenthal, G., Miley, G., 1979, A&A, 80, 13
Blandford R. D., Payne D. G., 1982, MNRAS, 199, 833
Bock D. C-J., Large M. I., Sadler E. M., 1999, AJ 117, 1578
Bremer M. N., Fabian A. C., Crawford C. S., 1997, MNRAS, 284, 213
Broderick J. W., Bryant J. J., Hunstead R. W., Sadler E. M., Murphy T., 2007 MNRAS, 381, 341 (Paper I)
Brookes M. H., Best P. N., Rengelink R., Röttgering H. J. A., 2006, MNRAS, 366, 1265
Brookes M. H., Best P. N., Peacock M. H., Röttgering H. J. A., Dunlop J. S., 2008, MNRAS, 385, 1297
Bryant J. J., Hunstead R. W., 2000, ApJ, 545, 216
Bryant J. J., Johnston H. M., Broderick J. W., Hunstead R. W., De Breuck C., Gaensler B. M., 2008, MNRAS submitted (Paper III)
Burgess A. M., Hunstead R. W., 2006, AJ, 131, 114
Carilli C. L., Röttgering H. J. A., van Ojik R., Miley G. K., van Breugel W. J. M., 1997, ApJS, 109, 1
Carilli C. L., Röttgering H. J. A., Miley G. K., Pentericci L. H., Harris D. E., 1999, in Röttgering H. J. A., Best P. N., Lehnert M. D., eds, The Most Distant Radio Galaxies, Netherlands Academy of Arts and Sciences, Amsterdam, p. 123
Chambers K.C., Miley G.K., van Breugel W.J.M., 1987, Nat, 329, 604
Condon J.J., Cotton W. D., Greisen E. W., Yin Q. F, Perley R. A., Taylor G. B., Broderick J. J., 1998 AJ 115, 1693
Croft S. et al., 2006, ApJ, 647, 1040
Croston J. H., Hardcastle M. J., Harris D. E., Belsole E., Birkinshaw M., Worrall D. M., 2005, ApJ, 626, 733
Cruz M. J. et al., 2006, MNRAS, 373, 1531
De Breuck C., van Breugel W., Röttgering H. J. A., Miley G., 2000, A&AS, 143, 303
De Breuck C., et al., 2001, AJ, 121, 1241
De Breuck C., van Breugel W., Stanford S.A., Röttgering H. J. A., Miley G., Sterm D., 2002, AJ, 123, 637
De Breuck C., Hunstead R. W., Sadler E. M., Rocca-Volmerange B., Klamer I., 2004, MNRAS 347, 837
De Breuck C., Klamer I., Johnston H., Hunstead R. W., Bryant J. J., Rocca-Volmerange B., Sadler E. M., 2006, MNRAS, 366, 58
Dunlop J., Peacock J.A.. 1993, MNRAS, 263, 936
Eales S., Rawlings S., Law-Green D., Cotter G., Lacy M., 1997, MNRAS, 291, 593.
Gebhardt K. et al., 2003 ApJ, 583, 92.
Gillingham P. Jones D., 2000, in Masanori I., Moorwood A. F. M., eds., Proc. SPIE: Optical and IR Telescope Instrumentation and Detectors, 4008, 1084.
Gooch R. 1996, in Jacoby G. H., Barnes J., eds, ASP Conf. Ser. 101: Astronomical Data Analysis Software and Systems V, 101, 80
Gopal-Krishna, 1988, A&A, 192, 37
Hambly N. C. et al., 2001, MNRAS, 326, 1279.
Kellermann K. I., Pauliny-Toth I. I. K., Williams P. J. S., 1969, ApJ, 157, 1
Klamer I., Ekers R. D., Sadler E. M., Hunstead R. W., 2004, ApJ, 612, L97
Klamer I., Ekers R. D., Bryant J. J., Hunstead R. W., Sadler E. M., De Breuck C., 2006, MNRAS, 371, 852
Laing R. A., Peacock J. A., 1980, MNRAS, 190, 903
Laing R. A., Riley J. M., Longair M. S., 1983, MNRAS, 204, 151
Large, M. I., Mills B. Y., Little A. G., Crawford D. F., Sutton J. M., 1981 MNRAS, 194, 693
Lilly S. J., Longair M. S., 1984, MNRAS, 211, 833
Martini P., Persson S. E., Murphy D. C., Birk C., Schectman S. A., Gunnels S. M., Koch E., 2004, in Moorwood A. F. M., Masanori I., eds, Proc SPIE: Ground-based Instrumentation for Astronomy, 5492, 1653
Matthews T. A., Morgan W. W., Schmidt M., 1964, ApJ, 140, 35
Mauch T., Murphy T., Buttery H. J., Curran J., Hunstead R. W., Piestrzynski B., Robertson J. G., Sadler E., 2003 MNRAS 342, 1117
McCarthy P.J., van Breugel W., Spinrad H., Djorgovski S., 1987, ApJ, 321, L29
McCarthy P.J., Kapahi, V. K., van Breugel W., Persson S. E., Athreya R. M., Subrahmanya C. R., 1996, ApJS, 107, 19
Miley G., De Breuck C., 2008 A&AR 15, 67
Owen F. N., Ledlow M. J., 1997, ApJS, 108, 41
Pentericci, L., Röttgering H. J. A., Miley G., Spinrad H., Mc Carthy P. J., van Breugel W. J. M., Macchetto F., 1998, ApJ, 504, 139
Pentericci, L., Mc Carthy P. J., Röttgering H. J. A., Miley G., van Breugel W. J. M., Fosbury R., 2001, ApJS, 135, 63
Rocca-Volmerange B., Le Borgne D., De Breuck C., Fioc M., Moy E., 2004, A&A, 415, 931
Röttgering H. J. A., Daddi E., Overzier R., Wilman R., 2003, NewAR, 47, 309
Sault R. J., Teuben P. J., Wright M. C. H., 1995, in Shaw R. A., Payne H. E., Hayes J. J. E., eds, ASP Conf. Ser. 77: Astronomical Data Analysis Software and Systems IV, 77, 433
Seymour N. et al., 2007, ApJS 171, 353

Skrutskie M. F. et al., 2006, AJ, 131, 1163
Tielens A., Miley G., Willis A., 1979, A&AS, 35, 153
van Breugel W. J. M., Stanford S. A., Spinrad H., Stern D., Graham J. R., 1998, ApJ, 502, 614
Venemans B. P. et al., 2007, A&A, 461, 823
White R. L., Becker R. H., 1992, ApJS, 79, 331
Willott C., Rawlings S., Jarvis M., Blundell K. 2003, MNRAS, 339, 173
Zirm A. W., Dickinson M., Dey A., 2003, ApJ, 585, 90

APPENDIX

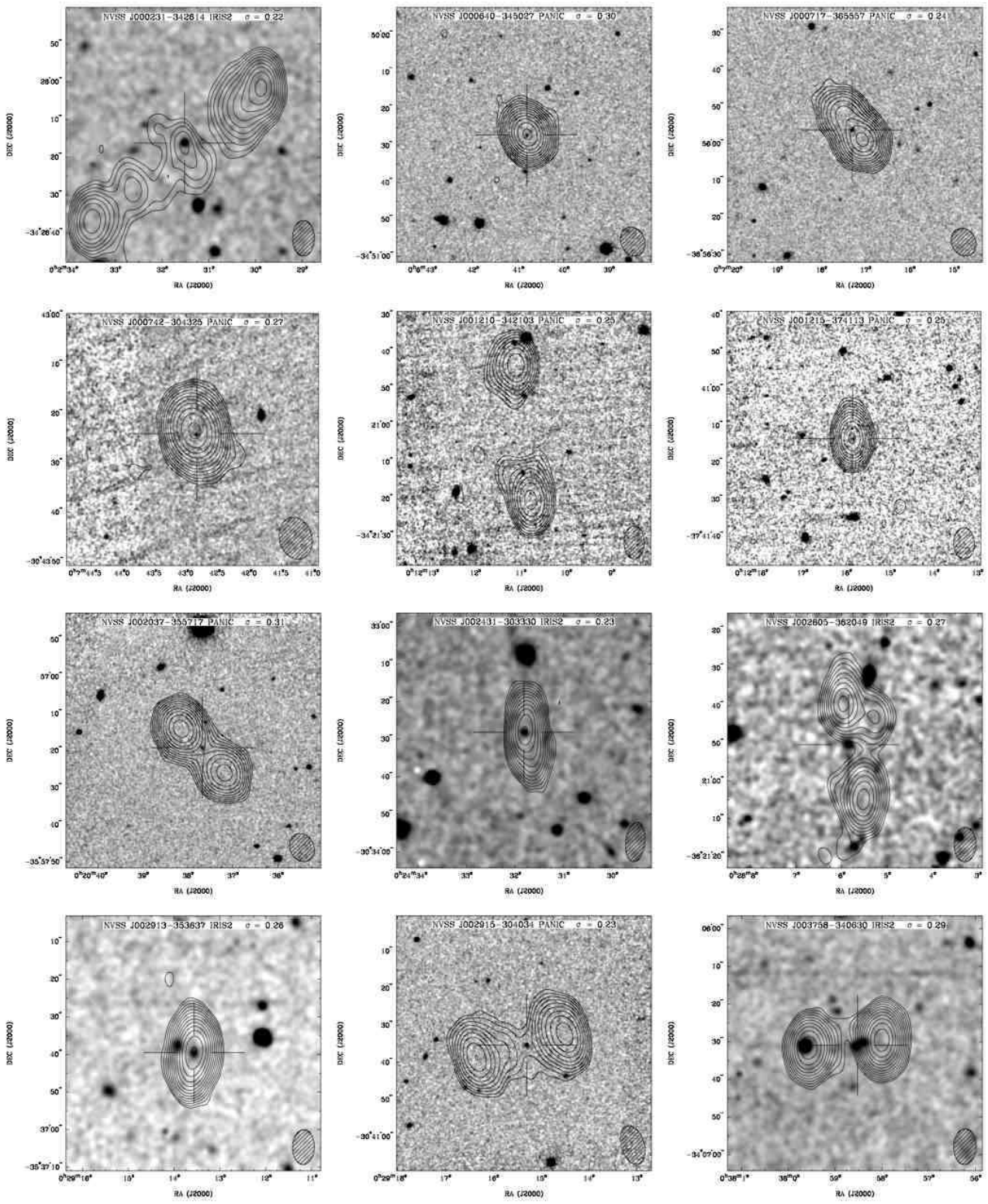

Figure A-1. 2368-MHz ATCA contours overlaid on the K-band images for all the sources in our sample that have IRIS2 or PANIC images and are not shown in Fig. 2. The full set of Appendix images are included in the MNRAS online journal. The K-band images show which instrument they are from, in the header, and they have been smoothed using a gaussian kernel of 3 pixels FWHM. All the radio contours are from natural-weighted images. The lowest contour is 3 sigma, and the contours are a geometric progression in $\sqrt{2}$. The rms noise (σ) is shown in the header of each image in mJy beam^{-1}. Crosshairs mark the K-band counterpart to the radio source. that were identified in K. The ATCA synthesized beam is shown in the bottom right-hand corner of each panel.

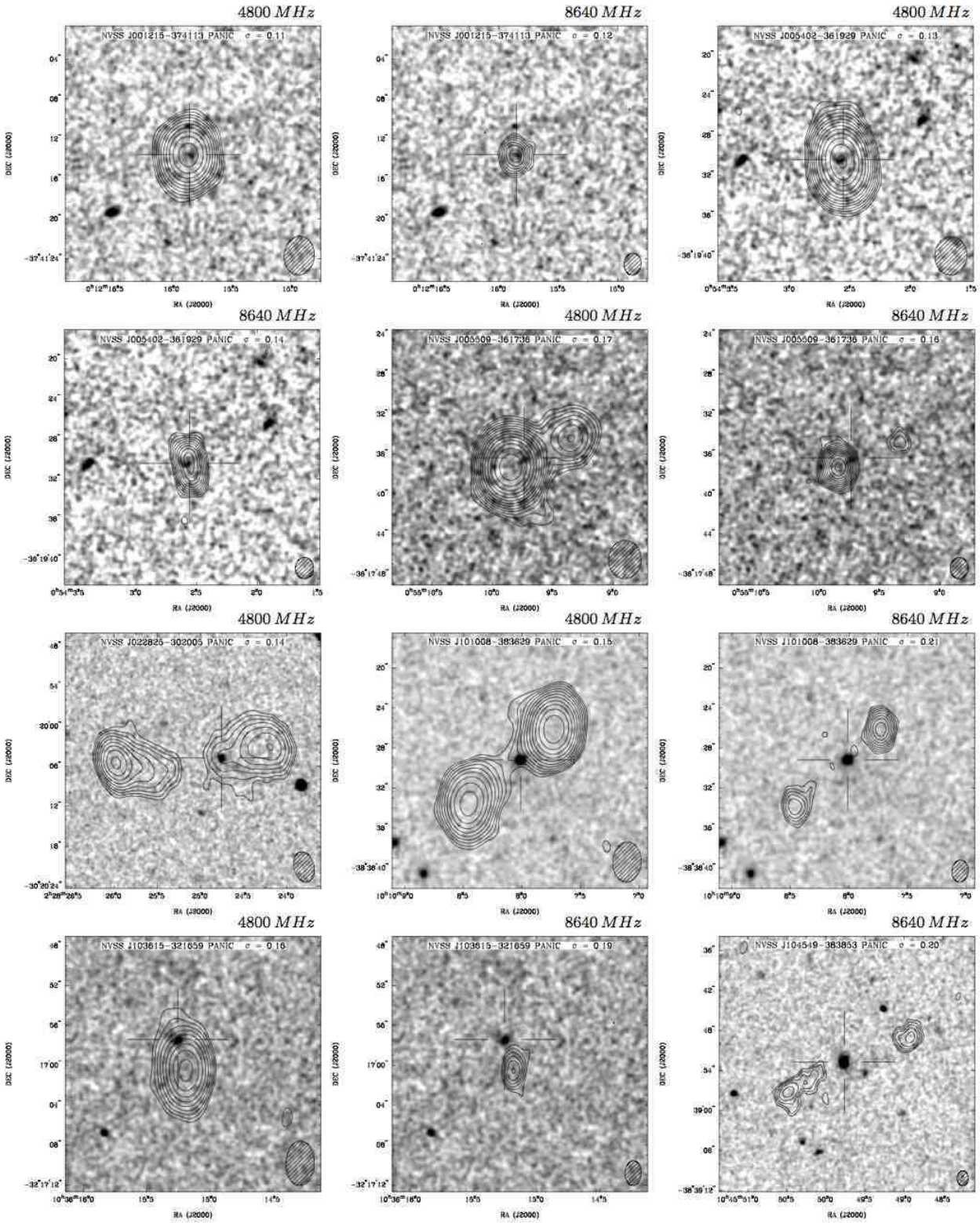

Figure A-2. K-band images for all the sources in our sample that have ATCA images at 4800- or 8640-MHz including all the images not already shown in Fig. 3. The full set of Appendix images are included in the MNRAS online journal. The frequency of the overlaid contours is marked on the top right of each image. The K-band images show which instrument they are from, in the header, and they have been smoothed using a gaussian kernel of 3 pixels FWHM. All the radio contours are from natural-weighted images. The lowest contour is 3 sigma, and the contours are a geometric progression in $\sqrt{2}$. The rms noise (σ) is shown in the header of each image in mJy beam^{-1}. Crosshairs mark the K-band counterpart to the radio source. that were identified in K. The ATCA synthesized beam is shown in the bottom right-hand corner of each panel.